

GOVERNMENT LICENSE

The submitted manuscript has been created by UChicago Argonne, LLC, Operator of Argonne National Laboratory (“Argonne”). Argonne, a U.S. Department of Energy Office of Science laboratory, is operated under Contract No. DE-AC02-06CH11357. The U.S. Government retains for itself, and others acting on its behalf, a paid-up nonexclusive, irrevocable worldwide license in said article to reproduce, prepare derivative works, distribute copies to the public, and perform publicly and display publicly, by or on behalf of the Government. The Department of Energy will provide public access to these results of federally sponsored research in accordance with the DOE Public Access Plan. <http://energy.gov/downloads/doe-public-access-plan>.

AlphaDiffract: Automated Crystallographic Analysis of Powder X-ray Diffraction Data

Nina Andrejevic^{1*†}, Ming Du^{1*†}, Hemant Sharma¹, James P. Horwath¹, Aileen Luo¹, Xiangyu Yin¹, Michael Prince¹, Brian H. Toby¹, and Mathew J. Chelukara^{1*}

¹*Advanced Photon Source, Argonne National Laboratory, Lemont, IL 60439, USA*

[†]Co-first authors with equal contribution.

*E-mail: nandrejevic@anl.gov, mingdu@anl.gov, mcherukara@anl.gov

ABSTRACT

Materials identification and structural understanding from powder X-ray diffraction (PXRD) data is a long-standing challenge in materials science, fundamental to discovering and characterizing novel materials. A prerequisite for full structure solution is the accurate determination of the crystal lattice, including lattice parameters and crystallographic symmetries. Traditional methods for this are iterative and typically require expert input, and while existing deep learning approaches have shown promise, a robust, single-shot method for comprehensive lattice determination from experimental data remains a key goal. Here, we introduce AlphaDiffract, a deep learning framework that achieves state-of-the-art performance in predicting the crystal system, space group, and lattice parameters directly from PXRD patterns. AlphaDiffract utilizes a 1D adaptation of the ConvNeXt architecture, a modern convolutional neural network that integrates key design principles from transformers, coupled with dedicated prediction heads for each crystallographic property. The model is trained on the largest-to-date physics-based dataset of over 31 million simulated diffraction patterns, generated by augmenting 312,267 curated structures from the ICSD and Materials Project databases. Crucially, it demonstrates strong generalization to experimental data, achieving 81.7% crystal system accuracy and 66.2% space group accuracy on the RRUFF dataset while additionally predicting all six lattice parameters. By providing a unified model for rapid and accurate lattice determination from PXRD data, AlphaDiffract represents a significant step forward in leveraging deep learning for high-throughput materials discovery.

1 Introduction

Powder X-ray diffraction (PXRD) is a fundamental characterization technique in materials science, essential for the discovery and understanding of novel materials. Determining the crystal lattice, which decodes the 1D diffraction pattern into the 3D unit cell geometry, is often a prerequisite for full structure solution from PXRD data [1]. While this is routine for single-crystal measurements, powder diffraction presents significant challenges. Traditional indexing algorithms can accomplish this for high-quality data [2–4], and experimental advances have further improved reliability; for instance, synchrotron sources eliminate sample offset uncertainties, while high-resolution measurements enable accurate determination of peak positions even for closely spaced reflections [5]. Once lattice parameters have been determined, probabilistic methods can assist in identifying the compatible space group from systematic absences and reflection conditions [6]. However, these methods still struggle in many realistic scenarios, particularly when materials contain impurities or when experimental conditions introduce peak broadening and overlap.

Recent deep learning approaches have demonstrated promise for automated crystallographic analysis from PXRD data. Convolutional neural networks (CNNs) are the most widely adopted architecture [7–16] as they capture both local peak features and global pattern structure through multiscale receptive fields. Alternative architectures such as multi-layer perceptrons [8, 11, 17] and transformers [11] have also been explored. These methods typically train on large synthetic datasets generated from crystallographic databases such as ICSD [18] and Materials Project [19], often incorporating data augmentation strategies to improve robustness [12, 15]. The RRUFF database of predominantly experimental patterns [20] has emerged as a key benchmark for evaluating generalization to real-world data [8, 12, 15, 16]. More recently, generative approaches, including large language models [21, 22] and diffusion models [16], have been applied

to obtain full structure predictions from PXRD patterns, though the former depend sensitively on knowledge of the chemical formula while the latter require separate predictions of the composition and lattice parameters.

Despite this progress, significant challenges remain for lattice determination from PXRD data. Supplementary Table 1 provides a detailed comparison of recent PXRD-based prediction methods, highlighting their architectures, training data sources, and predicted outputs. Most existing work focuses only on crystal system and space group classification [7–9, 12, 13, 15]. Approaches that predict lattice parameters either train separate models for each Bravais lattice or crystal system [10, 17], requiring prior symmetry knowledge, or depend on chemical composition as input and require subsequent refinement for experimental data [14]. Moreover, models trained primarily on idealized synthetic data frequently struggle with realistic experimental conditions, including noise, peak broadening, and instrumental effects. A unified framework that simultaneously predicts crystal system, space group, and lattice parameters while maintaining robust performance on experimental data remains an open challenge.

To address these challenges, we present AlphaDiffract, a unified deep learning framework for lattice determination from PXRD patterns. Our approach achieves state-of-the-art performance on the RRUFF dataset, reaching 81.7% crystal system accuracy and 66.2% space group accuracy while simultaneously predicting all six lattice parameters. Building on insights from prior work, our framework incorporates three key innovations:

1. While CNNs remain a popular and effective choice for analyzing sequential scientific data like PXRD patterns, creating an architecture that both excels at identifying local features, such as individual diffraction peaks, and captures the complex, long-range dependencies that encode crystallographic symmetry is challenging. To address this, we employ a 1D adaptation of the ConvNeXt architecture [23]. ConvNeXt is a modern CNN architecture adapted from ResNet [24], incorporating key design features of transformers that improve the parameter efficiency and modeling of long-range interactions. These improvements make ConvNeXt well-suited for PXRD data analysis, as the architecture inherits key strengths of transformers for processing sequential data while maintaining the spatial inductive biases that make CNNs effective for pattern recognition.
2. Our model is trained on simulated PXRD patterns generated using a combination of structures from the ICSD and Materials Project databases, reserving the RRUFF database as an independent benchmark for evaluating generalization. Following the curation process detailed in Methods Section 5.1, our combined ICSD and Materials Project dataset consists of 312,267 crystal structures. For each structure, we simulated 100 augmented diffraction patterns with randomized perturbations mimicking physical effects such as microstrain and crystallite size broadening (see Section 2.1). This data augmentation strategy produced a final training set of over 31 million diffraction patterns, making it, to our knowledge, the largest and most comprehensive dataset ever compiled for this task.
3. A key design feature of our approach is a single, end-to-end model that simultaneously predicts the crystal system, space group, and lattice parameters from the PXRD pattern alone. This unified architecture streamlines the crystallographic analysis pipeline, removing the need for separate, specialized models for each task and enabling complete lattice determination in a single inference step.

In the following sections, we detail our data generation pipeline, model architecture and training, and comprehensive evaluation on simulated and experimental benchmark datasets.

2 Results

2.1 Data preparation and physics-based simulation

To generate powder diffraction patterns matching experimental results, we used the GSAS-II crystallographic package via the GSASIIscriptable API [25, 26]. Since GSAS-II is designed for Rietveld analysis, it provides quantitatively accurate simulations of real instrumental data. Patterns were simulated for structures from the NIST ICSD database [27] and the Materials Project [19] to create our training dataset. All simulations employed a monochromatic X-ray source with 20 keV energy over a 2θ range of 5° to 20° with 8192 equally spaced points. To desensitize the model to experimental parameters that vary between diffraction instruments, we generated 100 different simulations per structure with randomized instrumental and sample parameters. Values for microstrain and crystallite size (both contributing Lorentzian broadening) and Gaussian instrumental broadening parameters were randomly sampled for each simulation within the ranges listed in Table 5, producing heterogeneous peak shapes representative of diverse experimental conditions [28]. During training, additional Poisson and Gaussian noise was applied dynamically to each pattern as detailed in Methods Section 5.2, and the intensities were subsequently standardized between 0 and 100 prior to being input to the model.

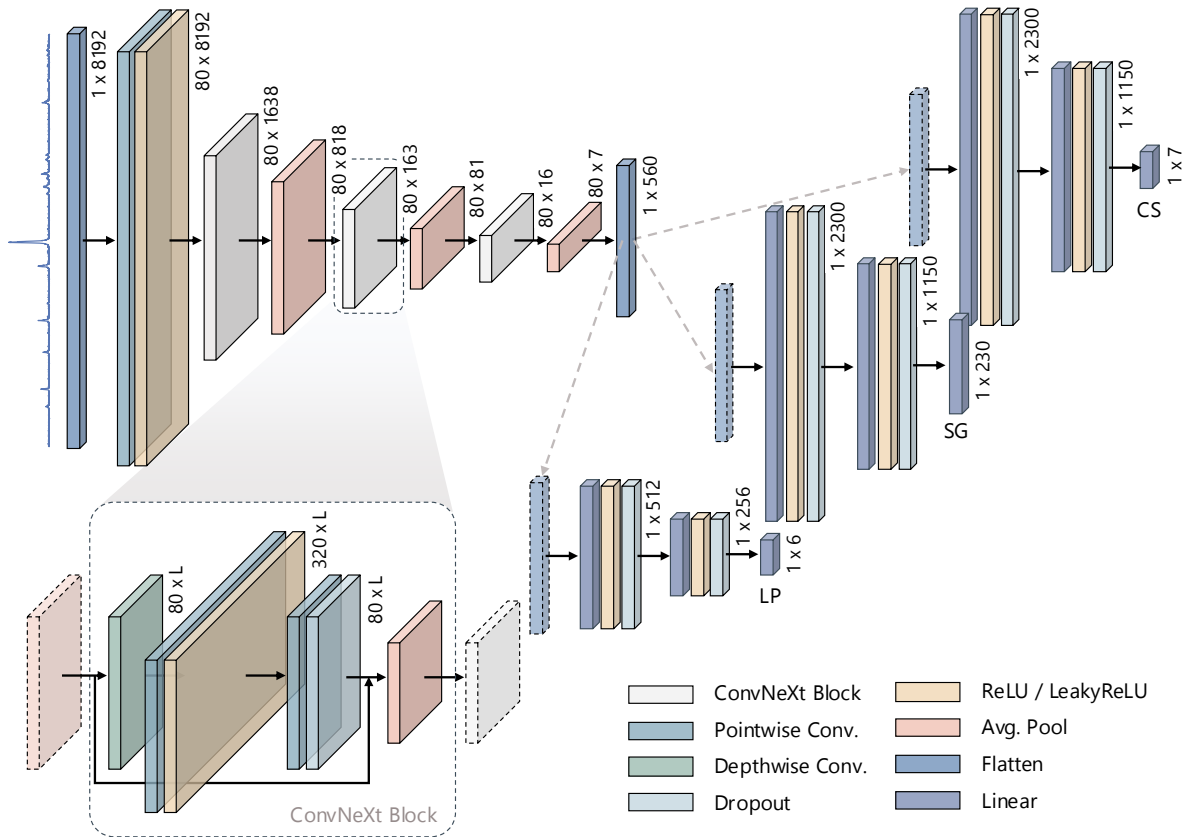


Figure 1: **AlphaDiffract model architecture.** The AlphaDiffract model consists of a 1D ConvNeXt backbone that processes input PXR D patterns through a series of ConvNeXt blocks with progressive downsampling. The composition of each ConvNeXt block is indicated in the bottom left inset. The extracted features are fed into three separate prediction heads: a crystal system (CS) classifier, a space group (SG) classifier, and a lattice parameter (LP) regressor. Each head employs a multi-layer perceptron architecture with layer dimensions as indicated.

2.2 AlphaDiffract architecture

The AlphaDiffract model extracts crystallographic information from a PXR D pattern through a 1D ConvNeXt backbone coupled with three specialized prediction heads. As illustrated in Figure 1, the backbone serves as a feature extractor that feeds into three distinct multilayer perceptron (MLP) heads for targeted predictions. The end-to-end model allows for the simultaneous prediction of the crystal system (CS), space group (SG), and all six lattice parameters (LP). The lattice parameters used for both model training and evaluation are those of the Niggli-reduced cell. The Niggli reduction provides a unique, canonical cell representation and thereby avoids ambiguity arising from different choices of unit cell setting.

The feature extractor is a 1D adaptation of the ConvNeXt architecture [23], a convolutional neural network (CNN) that incorporates principles from vision transformers, such as depthwise separable convolutions, an inverted bottleneck design, and large kernel sizes. The input PXR D pattern, a 1×8192 vector, is processed through a series of ConvNeXt blocks. Each block, shown in the inset of Figure 1, uses a depthwise convolution to capture spatial patterns (*i.e.*, peak shapes and local arrangements) followed by pointwise convolutions to learn channel-wise interactions. This structure is parameter-efficient for modeling relationships across the pattern. After each block, average pooling progressively downsamples the feature map, increasing the network’s receptive field and enabling it to capture long-range dependencies between distant diffraction peaks. The final output of the backbone is a 560-dimensional feature vector that encodes key features from the raw diffraction pattern to enable the downstream classification and regression tasks.

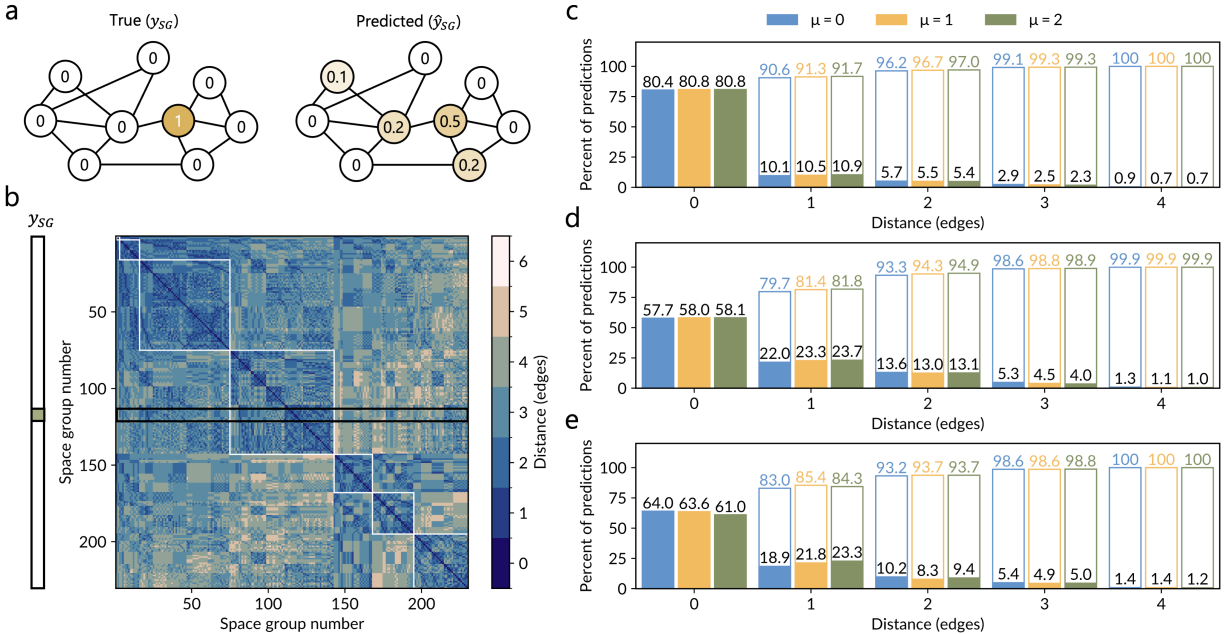


Figure 2: **Evaluation of space group predictions using Graph Earth Mover’s Distance.** **a**. Illustration of true (y_{SG}) and predicted (\hat{y}_{SG}) space group probability distributions on a representative subgroup graph, where nodes represent space groups and edges indicate maximal subgroup relationships. The true label assigns probability 1 to a single node (yellow), while the predicted distribution typically spreads probability across multiple nodes. **b**. Distance matrix computed from maximal subgroup relationships between space groups, where color intensity indicates the minimum number of graph edges connecting each pair of space groups. The vertical vector (y_{SG}) represents a one-hot encoded true label that selects the corresponding row for calculating the GEMD loss against predicted distributions. **c-e**. Distribution of prediction errors as a function of graph distance (number of edges) from the true space group for three datasets: **c**. ICSD validation set, **d**. Materials Project validation set, and **e**. RRUFF test set. Filled bars show the percentage of all predictions (including correct predictions at distance 0) that fall at each graph distance from the true space group, for three different GEMD loss weights ($\mu = 0, 1, 2$). Distance zero indicates a correct prediction (predicted space group = true space group). Unfilled bars with labeled values indicate the corresponding cumulative percentages up to and including that distance. With higher μ values, predictions become increasingly concentrated at shorter graph distances from the true space group.

This feature vector is passed to three specialized MLP prediction heads, each tailored for a specific task: a 7-node output for crystal system classification, a 230-node output for space group classification, and a 6-node output for lattice parameter regression. This multi-task approach allows the model to learn shared representations in the backbone while fine-tuning the predictions for each distinct crystallographic property. Details on the architectural parameters can be found in Methods Section 5.3.

2.3 Physics-aware loss function

A key innovation in AlphaDiffraXt is a novel loss function for space group classification in addition to standard cross-entropy. While cross-entropy penalizes all misclassifications equally, space groups are structurally related through symmetry hierarchies where closely related sub- or supergroups are more similar, making some misclassifications less severe than others. To incorporate these relationships, we implement a Graph Earth Mover’s Distance (GEMD) loss which adapts the traditional Earth Mover’s Distance to the maximal subgroup graph, where nodes represent space groups and edges connect groups with direct maximal subgroup relationships, reflecting their structural similarity. This approach was inspired by the work of Vecsei *et al.* that evaluated space group prediction performance using maximal subgroup distance as a metric [29] but further develops this concept into a loss function that enforces these structural relationships during training. The GEMD loss uses a pre-computed 230×230 distance matrix D , where each element D_{ij} encodes the number of hops between space groups i and j through this graph (Figure 2a and b), which were determined using the MAXSUB program [30] available on the Bilbao Crystallographic Server [31]. As illustrated in

Figure 2a, the true label assigns probability 1 to a single space group, while the predicted distribution typically spreads probability across multiple nodes. The GEMD loss calculates the cost to transport probability mass from the predicted distribution to the true distribution, where this cost is weighted by the distances in matrix D . This approach penalizes misclassifications based on their crystallographic dissimilarity, as predictions that are further from the true space group in the subgroup graph incur a larger penalty. The loss function includes a hyperparameter μ that controls the weight of the GEMD term relative to cross-entropy, allowing us to balance the two objectives during training. Additional details about the loss functions are provided in Methods Section 5.4.

To determine the optimal weight for the GEMD loss term, we trained models with only the crystal system and space group prediction heads (excluding lattice parameters) using three different values of μ (0, 1, 2), where $\mu = 0$ corresponds to standard cross-entropy alone. We evaluate these models on our primary RRUFF test set as well as on the ICSD and Materials Project validation sets (Figures 2c-e). In these figures, a graph distance of zero indicates an exact correct prediction; non-zero distances reflect misclassifications where the predicted space group is crystallographically separated from the true space group by the indicated number of edges in the subgroup graph. We find that incorporating the GEMD loss shifts the error distribution toward shorter graph distances from the true space group; that is, when the model is wrong, it tends to predict space groups that are crystallographically close to the true space group in the subgroup hierarchy. This pattern is consistent across the RRUFF test set as well as the ICSD and Materials Project validation sets. The cumulative percentages demonstrate that with $\mu = 1$, over 85% of predictions on RRUFF are correct or differ by a single symmetry generator (are within 1 edge) of the true space group. Based on these results, we select $\mu = 1$ for training the full model with all three prediction heads.

2.4 AlphaDiffract performance on classification tasks

Having established $\mu = 1$ as the optimal GEMD loss weight, we trained a 10-model ensemble with all three prediction heads (crystal system, space group, and lattice parameters). Figure 3a shows that both crystal system and space group accuracies on RRUFF improve with ensemble size with diminishing returns beyond 8-10 models, justifying our choice of a 10-model ensemble. Tables 1 and 2 summarize the classification performance across three datasets for the classification-only model (Cls.) and joint classification and regression models (Cls. + Regr.), reporting both the independent results of the 10 models (averaged) and the ensemble results obtained by aggregating their predictions. We also include the baseline performance from a naive majority-class classifier for reference. On our RRUFF test set, our ensemble model achieves crystal system and space group classification accuracies of $81.74 \pm 0.78\%$ and $66.21 \pm 0.71\%$, respectively, where uncertainties represent the combined effect of ensemble and augmentation variability (see Methods Section 5.6). These results substantially exceed the baseline accuracies of 26.98% and 3.27%, respectively, demonstrating that the model has learned meaningful crystallographic patterns rather than exploiting class imbalances. The results also compare favorably to prior work evaluated on RRUFF data. For crystal system classification, our ensemble model outperforms Lee *et al.*'s Large FCN (74.24%) [12] and Salgado *et al.*'s NPCNN (74%) [15], while for

	Model Variant	ICSD	Materials Project	RRUFF
	Baseline	20.13	20.63	26.98
	Park <i>et al.</i> [7]	94.99	–	–
	Vecsei <i>et al.</i> [8]	Dense	73	–
	Vecsei <i>et al.</i> [8]	Convolutional	85	–
	Lee <i>et al.</i> [11]	FCN	92.12	82.17
	Lee <i>et al.</i> [12]	Large FCN	92.10	–
	Salgado <i>et al.</i> [15]	Large, NPCNN	–	–
	Choudhary [21]	DGPT-formula	18.16 (19.80) [†]	30.10 (32.10) [†]
	Ours	Cls. ($\mu = 1$)	90.60 \pm 0.38 [†]	76.75 \pm 0.60 [†]
	Ours	Cls. + Regr. (Avg.)	90.52 \pm 0.38 [†]	76.47 \pm 0.60 [†]
	Ours	Cls. + Regr. Ensemble	92.22 \pm 0.40 [†]	79.00 \pm 0.64 [†]
				81.74 \pm 0.78[‡]

Table 1: **Crystal system classification accuracies of AlphaDiffract and reference models.** Some referenced works trained multiple models with different architectures and/or datasets, for which we only show the model variant giving the best result without including RRUFF data in its training set. “Baseline” denotes a naive classifier that always predicts the most abundant class in the training data. For our approach, “Avg.” denotes the average independent performance of 10 trained models, while “Ensemble” refers to the ensemble-averaged prediction from these models. Error bars represent the aggregated 95% confidence intervals of the ensemble and augmentation uncertainties.

[†]Evaluated on our validation set data. For inference with the DGPT-formula model in Ref. 21, 1000 representative examples from the validation set of each dataset were selected for evaluation. Scores in parentheses refer to results on synthetic PXRD patterns with no added Poisson or Gaussian noise.

[‡]Evaluated on our test set data.

	Model Variant	ICSD	Materials Project	RRUFF
	Baseline	7.01	6.36	3.27
	Park <i>et al.</i> [7]	81.14	–	–
	Vecsei <i>et al.</i> [8]	Dense	57	54
	Vecsei <i>et al.</i> [8]	Convolutional	76	42
	Liang <i>et al.</i> [17]	–	78.77*	–
	Lee <i>et al.</i> [11]	FCN	79.67	69.01
	Lee <i>et al.</i> [12]	Large FCN	84.85	58.82
	Salgado <i>et al.</i> [15]	Large, NPCNN	–	66
	Choudhary [21]	DGPT-formula	3.99 (5.43) [†]	5.46 (5.48) [‡]
	Ours	Cls. ($\mu = 1$)	80.79 \pm 0.54 [†]	63.62 [‡]
	Ours	Cls. + Regr. (Avg.)	79.96 \pm 0.55 [†]	64.55 [‡]
	Ours	Cls. + Regr. Ensemble	81.75 \pm 0.59	66.21 \pm 0.71[‡]

Table 2: **Space group classification accuracies of AlphaDiffract and reference models.** Some referenced works trained multiple models with different architectures and/or datasets, for which we only show the model variant giving the best result without including RRUFF data in its training set. “Baseline” denotes a naive classifier that always predicts the most abundant class in the training data. For our approach, “Avg.” denotes the average independent performance of 10 trained models, while “Ensemble” refers to the ensemble-averaged prediction from these models. Error bars represent the aggregated 95% confidence intervals of the ensemble and augmentation uncertainties.

*Weighted average over models specialized for each Bravais lattice.

[†]Evaluated on our validation set data. For inference with the DGPT-formula model in Ref. 21, 1000 representative examples from the validation set of each dataset were selected for evaluation. Scores in parentheses refer to results on synthetic PXRD patterns with no added Poisson or Gaussian noise.

[‡]Evaluated on our test set data.

space group classification, it surpasses Lee *et al.*’s Large FCN (58.82%) and performs comparably to Salgado *et al.*’s NPCNN (66%).

For comparison with models evaluated primarily on synthetic data, we also report results on our ICSD and Materials Project validation sets, where our ensemble model achieves crystal system accuracies of $92.22 \pm 0.40\%$ and $79.00 \pm 0.64\%$, and space group accuracies of $81.75 \pm 0.59\%$ and $59.54 \pm 0.79\%$, respectively. Several prior works achieve slightly higher accuracies on ICSD synthetic data, including Park *et al.* (94.99% CS) [7] and Lee *et al.* (84.85% SG) [12], and outperform our model on Materials Project synthetic data, *e.g.* Lee *et al.* (82.17% CS, 69.01% SG) [11]. However, these comparisons should be interpreted with consideration of the data generation procedures used for training. Our training data includes extensive augmentation spanning wide ranges of sample and instrument broadening parameters, as well as realistic Poisson and Gaussian noise levels derived from RRUFF patterns (Table 5 and Supplementary Figure 4). While some prior works describe parameter variation in their synthetic data generation, the specific ranges and noise models used are not always fully specified in the literature, which can affect both training robustness and generalizability to experimental data. The performance gap between synthetic and experimental datasets – both in our work and in prior studies – underscores the challenge of accurately modeling the full complexity of real-world PXRD measurements. Notably, incorporating lattice parameter regression alongside classification (Cls. + Regr.) maintains or slightly improves classification performance compared to the classification-only model (Cls.), demonstrating that the additional regression task does not compromise classification accuracy. Ensembling 10 independently trained models (Cls. + Regr. Ensemble) further improves performance across all datasets, achieving our best results of 81.74% for crystal system and 66.21% for space group classification on RRUFF. Figure 3b shows the distribution of space group prediction errors as a function of graph distance for the ensemble model across all three datasets, demonstrating that the GEMD loss successfully concentrates errors at shorter distances from the true space group, with over 87% of predictions on RRUFF data falling within 1 edge of the true space group.

2.5 AlphaDiffract performance on regression tasks

For lattice parameter prediction, we evaluate the ensemble model’s regression performance across the same three datasets (Table 3, Figures 3c-e). As a reference, we also include the baseline performance from a naive model that predicts the average lattice parameters from the training data for all inputs. On RRUFF, the ensemble model achieves mean absolute errors (MAE) of $2.11 \pm 0.02 \text{ \AA}$ for lattice lengths and $2.72 \pm 0.03^\circ$ for lattice angles, with corresponding mean absolute percentage errors (MAPE) of $23.50 \pm 0.25\%$ and $2.91 \pm 0.03\%$, respectively, representing clear improvements over baseline predictions. The coefficients of determination (R^2) are 0.39 ± 0.01 for lengths and 0.25 ± 0.01 for angles. Metrics evaluated per lattice parameter are also reported in Supplementary Table 2. We note that while these results represent a clear improvement over the naive baseline and existing unified-model approaches, the

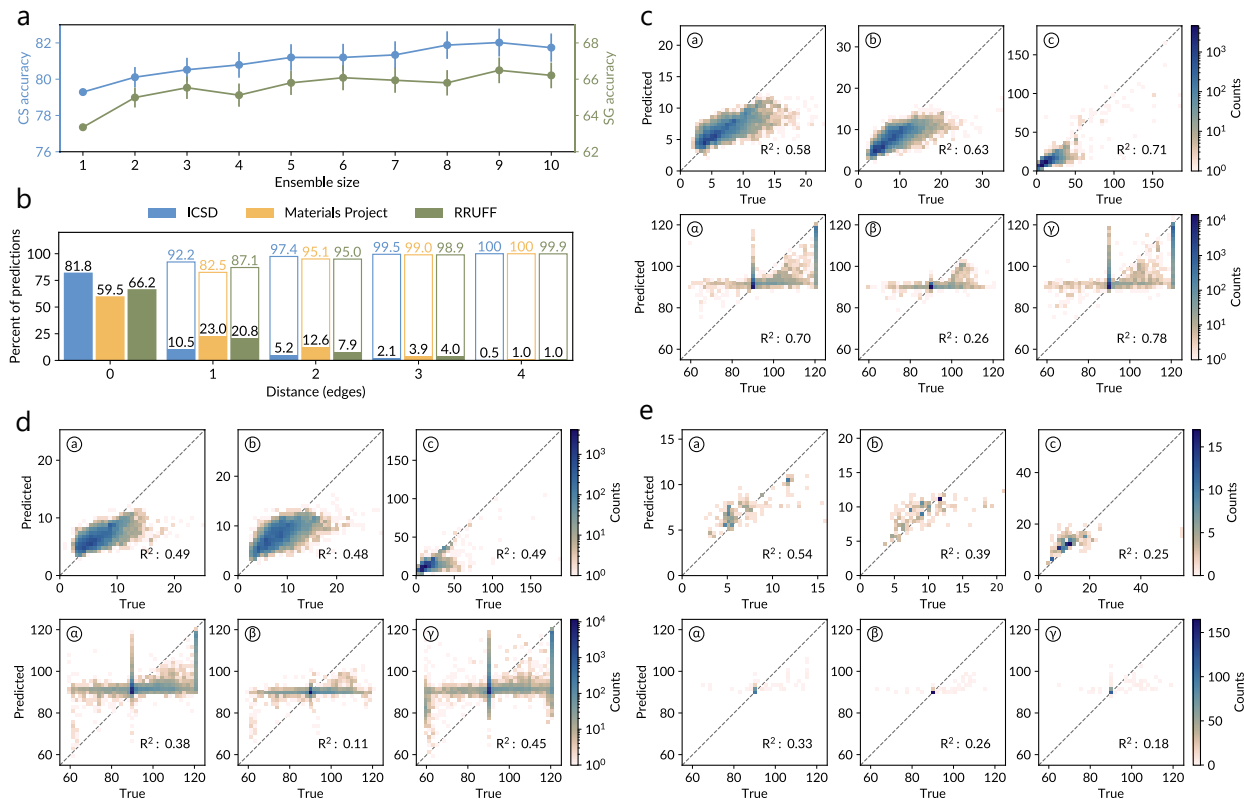


Figure 3: AlphaDiffract ensemble model performance. **a.** Crystal system (CS) and space group (SG) prediction accuracies on the RRUFF dataset as a function of ensemble size. Error bars represent the uncertainty in model predictions within the ensemble. **b.** Distribution of prediction errors as a function of graph distance (number of edges) from the true space group for the 10-model ensemble evaluated on the three datasets. Unfilled bars with labeled values indicate the cumulative percentage of predictions falling within that graph distance of the true space group (*i.e.*, the sum of all filled bars up to and including that distance). **c-e.** Parity plots comparing predicted versus true lattice parameters for the 10-model ensemble across three datasets: **c.** ICSD, **d.** Materials Project, and **e.** RRUFF. Each panel shows predictions for the three lattice lengths (a , b , c ; top row) and three lattice angles (α , β , γ ; bottom row). Dashed lines indicate perfect agreement. Heat map coloring represents point density. R^2 values indicate goodness of fit.

absolute accuracy, particularly the $\sim 20\%$ MAPE on lattice lengths, is not yet sufficient for direct use as an initializer for whole-pattern refinement methods such as Pawley or Le Bail fits, which typically require cell parameter accuracy within a few percent. AlphaDiffract’s predictions are therefore best interpreted as rapid, coarse estimates of the lattice that can guide subsequent refinement rather than replace it.

On synthetic data, the ensemble model also achieves strong performance, with MAE values of 1.59 Å and 1.68° ($R^2 = 0.64$ and 0.58 for lengths and angles) on ICSD, and 1.92 Å and 3.54° ($R^2 = 0.48$ and 0.32) on Materials Project. Chitturi *et al.* report lower MAPE (9.2%) on ICSD data; however, their approach trains separate models for each of the seven crystal systems. Since AlphaDiffract employs a single unified model for all crystal systems, it may better reflect practical application scenarios for lattice determination where the crystal system may not be known *a priori*. Figures 3c-e show parity plots comparing the lattice parameters predicted by the ensemble model against their ground truth values across all three datasets. The plots show that predictions are generally well-correlated with true values, though with greater scatter for RRUFF data compared to synthetic ICSD patterns. The R^2 values for lattice angles are notably lower than those for lattice lengths, which is explained by the fact that angles are constrained by symmetry to fixed values (e.g., 90°) for all crystal systems except monoclinic and triclinic. The model frequently predicts these fixed values correctly, producing the dense clusters visible in Figures 3c-e, but this simultaneously leads to low R^2 values as the metric measures explained variance. The performance gap between synthetic and experimental data for lattice

Dataset	Model	Lattice Length			Lattice Angle		
		MAE (Å)	MAPE (%)	R^2	MAE (°)	MAPE (%)	R^2
ICSD	Baseline	3.18	44.89	0.00	4.56	4.48	0.00
	Chitturi <i>et al.</i> [10]	–	9.2*	–	–	–	–
	Liang <i>et al.</i> [17]	–	–	0.45**	–	–	0.19**
	Choudhary [21]	2.85 (2.79) [†]	34.32 (33.66) [†]	-0.03 (-0.06) [†]	5.76 (6.23) [†]	5.82 (6.33) [†]	-2.07 (-2.80) [†]
	Ours	1.59 ± 0.00[†]	19.77 ± 0.04[†]	0.64 ± 0.00[†]	1.68 ± 0.01[†]	1.69 ± 0.01[†]	0.58 ± 0.00[†]
Materials Project	Baseline	2.89	34.76	-0.01	5.22	5.55	0.00
	Chitturi <i>et al.</i> [10]	–	–	–	–	–	–
	Liang <i>et al.</i> [17]	–	–	–	–	–	–
	Choudhary [21]	2.69 (2.69) [†]	28.14 (27.04) [†]	-0.01 (-0.01) [†]	5.97 (6.29) [†]	6.25 (6.61) [†]	-1.54 (-1.99) [†]
	Ours	1.92 ± 0.00[†]	22.59 ± 0.04[†]	0.48 ± 0.00[†]	3.34 ± 0.01[†]	3.61 ± 0.01[†]	0.32 ± 0.00[†]
RRUFF	Baseline	2.86	31.03	-0.08	4.19	4.49	-0.07
	Chitturi <i>et al.</i> [10]	–	–	–	–	–	–
	Liang <i>et al.</i> [17]	–	–	–	–	–	–
	Choudhary [21]	2.53 (2.40) [‡]	25.94 (25.32) [‡]	-0.11 (-0.12) [‡]	5.32 (5.39) [‡]	5.73 (5.72) [‡]	-2.34 (-2.31) [‡]
	Ours	2.11 ± 0.02[‡]	23.50 ± 0.25[‡]	0.39 ± 0.01[‡]	2.72 ± 0.03[‡]	2.91 ± 0.03[‡]	0.25 ± 0.01[‡]

Table 3: **Lattice parameter prediction errors of AlphaDiffract and reference models.** Errors are quantified in terms of the Mean Absolute Error (MAE), Mean Absolute Percentage Error (MAPE), and coefficient of determination (R^2). For direct comparison, we limit our analysis to studies that quantify prediction accuracy using regression metrics rather than classification metrics like match rate. Due to the scarcity of works tested on RRUFF, we also list those tested on other datasets for reference only. “Baseline” denotes a naive model that predicts the average lattice parameters from the training data for all inputs. Error bars represent the aggregated standard deviations in the predictions of the ensemble and augmentations.

*Weighted average over models specialized for each crystal system. Note these results correspond to a combined ICSD/CSD dataset.

**Weighted average over models specialized for each Bravais lattice.

[†]Evaluated on our validation set data. For inference with the DGPT-formula model in Ref. 21, 1000 representative examples from the validation set of each dataset were selected for evaluation. Scores in parentheses refer to results on synthetic PXRD patterns with no added Poisson or Gaussian noise.

[‡]Evaluated on our test set data.

parameter regression parallels that observed for classification, reflecting the increased difficulty of precise quantitative predictions from real-world measurements with complex experimental artifacts.

2.6 Inference time statistics

To evaluate the computational efficiency of our AlphaDiffract, we measured the inference times of individual models across the three evaluation datasets (Table 4). A single model achieves average inference times of 1.15-1.39 ms per PXRD pattern and median times of 1.04-1.08 ms across all datasets. These results correspond to an inference rate of 700-870 samples per second on a single GPU, making AlphaDiffract highly suitable for real-time analysis and ultrahigh-throughput screening applications. The consistency of inference times across datasets of varying sizes (734 to 10,000 samples) indicates stable performance regardless of dataset scale. For the ensemble approach using 10 models, inference time scales approximately linearly to 11.5-13.9 ms per pattern (70-90 samples/second), as predictions from each model are generated sequentially. Even with this tenfold increase, the ensemble inference time remains negligible compared to typical Rietveld refinement times of several seconds to minutes per pattern. This rapid inference enables both the single-model and ensemble approaches to serve as efficient preprocessing steps in automated Rietveld refinement pipelines, providing initial estimates of crystal system, space group, and lattice parameters without adding meaningful computational overhead to crystallographic workflows.

Dataset	Number of samples	Average time per sample (ms)	Median time per sample (ms)	Throughput (samples / s)
ICSD	10,000	1.33	1.08	751
Materials Project	10,000	1.39	1.08	719
RRUFF	734	1.15	1.04	871

Table 4: **Inference time statistics.** Per-model inference time statistics across evaluation datasets. All measurements performed on a single NVIDIA H100 GPU with batch size 1.

3 Discussion

Despite the strong performance of AlphaDiffract, several limitations present avenues for future improvement. A primary challenge is the inherent class imbalance within the training data. Crystallographic databases like ICSD and Materials Project are heavily skewed, with a few common space groups (*e.g.*, $P2_1/c$, $Pnma$) being vastly overrepresented, while dozens of others are rare. This imbalance, visible in Supplementary Figure 1, contributes to the performance disparity observed between datasets. As shown in Supplementary Figure 5, performance varies significantly across crystal systems, with cubic systems achieving the highest accuracy (99.7%, 99.3%, and 82.4% for crystal system prediction on ICSD, Materials Project, and RRUFF datasets, respectively, and 88.1%, 76.8%, and 78.2% for space group prediction, respectively) while lower-symmetry systems show more variable performance. Triclinic and monoclinic systems, which are among the most challenging, show notably lower accuracies across all datasets. The Materials Project contains a higher fraction of these lower-symmetry systems, many of which are computationally predicted or metastable structures less common in the training data, and this compositional difference translates directly into lower overall classification accuracy on this dataset. However, the skew towards more common, higher-symmetry space groups in the training data is also commensurate with the likelihood of encountering them in real materials.

Furthermore, the current model does not explicitly account for preferred orientation (texture), a common experimental artifact that significantly alters relative peak intensities. Since the model relies on the entire pattern, including intensities, it can be misled by experimental data with strong texture. Supplementary Figure 6 compares space group classification performance on experimental versus synthetic RRUFF patterns from the same crystal structures, showing that synthetic patterns achieve 15-17% higher accuracy than experimental patterns. This performance gap may be partly attributed to texture effects present in the experimental measurements but absent from our training data perturbations. For instance, attention analysis via GradCAM [32] (Supplementary Figures 7 and 8) reveals that the model sometimes focuses on very different pattern regions when processing experimental versus simulated data, particularly for structures exhibiting texture effects, suggesting the model adapts its classification strategy based on intensity variations. While our data augmentation provides some robustness, future iterations could benefit from incorporating texture simulation into the training data or designing the architecture to be less sensitive to intensity ratios.

Regarding lattice parameter prediction, we wish to emphasize that the reported errors ($\sim 20\%$ MAPE on lengths, $\sim 3\%$ MAPE on angles for RRUFF) represent a meaningful step toward unified lattice determination but fall short of the precision required for practical Rietveld refinement initialization. The performance gap relative to crystal-system-specialized approaches such as Chitturi *et al.* (9.2% MAPE) reflects the inherent difficulty of a fully unified model that must implicitly infer crystal system before predicting lattice parameters. Improving this accuracy, for example through a sequential or hierarchically conditioned architecture, is an important direction for further study.

Future work will focus on several directions. First, we plan to explore alternative architectures to improve multi-task learning. A branched, multi-task network, for example, could be trained sequentially, first to predict the crystal system and space group, and then to use that prediction to inform a more accurate, system-specific lattice parameter prediction. Finally, we anticipate that by introducing diffraction peaks at random locations into the training data, we can desensitize the model to the presence of additional phases, providing a unique tool that can index diffraction patterns from mixtures. Second, while our model predicts crystal system, space group, and lattice parameters, it does not yet determine atomic positions – the final step needed for complete end-to-end crystal structure determination from powder diffraction data. However, our work addresses critical subproblems within this broader challenge. Recent approaches have explored different paradigms for this inverse design problem. For instance, the Crystalyze model by Riesel *et al.* uses a diffusion model that requires accurate lattice parameters, composition, and number of atoms to initialize the unit cell before generating atomic positions [16]. AlphaDiffract’s lattice parameter predictions could enhance this initialization step, and the crystal system and space group predictions could be used to enforce symmetry constraints and guide the diffusion model toward atomic positions consistent with the underlying crystallographic symmetries. Alternative LLM-based approaches, such as DiffractGPT [21] and deCIFer [22], operate on different principles but accept optional conditioning information (*e.g.*, space group information for deCIFer) that our predictions could potentially enhance. Integration of our predictions with these generative approaches represents a promising direction for future work toward fully automated structure solution. Nonetheless, accurate prediction of lattice parameters, crystal system, and space group from experimental PXRD data alone, as demonstrated here, already addresses a fundamental bottleneck in crystallographic analysis. This capability enables rapid structural characterization without requiring prior knowledge of composition or separate models for different crystal systems, advancing the goal of high-throughput materials discovery.

4 Conclusion

We have presented AlphaDiffract, a unified deep learning framework for lattice determination from PXRD patterns. Leveraging a 1D ConvNeXt architecture and a physics-based training set of over 31 million simulated patterns

incorporating realistic experimental effects, AlphaDiffract simultaneously predicts crystal system, space group, and all six lattice parameters from a single diffraction pattern.

On the RRUFF benchmark, our ensemble model achieves 81.7% crystal system and 66.2% space group classification accuracy while simultaneously setting a new standard for lattice parameter regression from experimental PXRD data. This performance matches or exceeds prior state-of-the-art methods specialized for classification alone, demonstrating that unified prediction of symmetry and lattice parameters is feasible without compromising accuracy. Our physics-aware GEMD loss further concentrates prediction errors near the true space group in the symmetry hierarchy, providing crystallographically meaningful predictions even when exact matches are not achieved.

Determination of crystal structures from powder diffraction remains challenging, with existing *ab initio* methods limited by data quality requirements and restricted applicability [33–37]. AlphaDiffract addresses a critical component of this workflow by directly predicting lattice parameters and space group candidates from diffraction patterns alone, bypassing explicit peak finding and indexing steps. When predicted space groups differ from ground truth, they typically represent immediate subgroups or supergroups differing by a single symmetry generator, information that aids both conventional structure determination tools and crystallographic database searches [38]. As deep learning methods continue to mature and integrate with existing crystallographic workflows, they increasingly offer practical solutions to long-standing challenges in powder diffraction structure solution.

5 Methods

5.1 Data curation

Materials structures for training were downloaded as CIF files [39] from two major crystallographic databases: 198,778 structures from ICSD [27] and 153,169 structures from the Materials Project [19]. No attempts were made to prevent structure duplication. As a first refinement step, we ensured that all CIF files could be successfully parsed into `pymatgen` [40] structures to enable subsequent quality checks and the writing of Niggli reduced structures. This parsing step resulted in 186,765 validated structures from ICSD and 153,169 from the Materials Project.

The second stage of refinement applied several quality checks using `pymatgen`'s `SpacegroupAnalyzer` [40]. We confirmed that the space group of the conventional cell remained consistent across a range of site tolerances from 0.01 Å to 0.1 Å and angle tolerances from 0.1° to 5°, where the upper bounds represent the default values used by the Materials Project [40]. Additionally, we verified that the Niggli reduced cell was consistent with crystal system symmetry within a relative tolerance of 10^{-3} when comparing expected unit cell length and angle equivalences. We also applied practical constraints, requiring that structures have a unit cell volume less than 100,000 Å³ and contain no more than 500 atoms per unit cell. After applying these screening criteria, the final dataset consisted of 165,634 valid structures from ICSD and 146,633 from the Materials Project.

Materials structures and PXRD patterns for testing were downloaded from the RRUFF database [20], consisting of 1,362 PXRD patterns, which are background-corrected to flat baselines but otherwise unmodified, and 2,901 DIF files, which contain structural information obtained through refinement of the experimental PXRD patterns. The RRUFF patterns used in this study are the background-corrected versions provided directly by the RRUFF database, where backgrounds have been subtracted to produce flat baselines by the database curators. No additional background subtraction or processing was applied by the authors beyond the wavelength conversion described below. Initial screening removed DIF files lacking essential information (cell parameters, space group, or wavelength data), resulting in 2,572 valid files. Of these, 1,880 DIF files could be successfully parsed into `pymatgen` lattices, though not necessarily into full structures, as some lacked atom coordinates or contained non-standard atom symbols.

Further refinement verified that 1,867 structures had lattices consistent with crystal system symmetry within a relative tolerance of 10^{-3} (comparing expected unit cell length and angle equivalences) and a unit cell volume less than 100,000 Å³. Among these, 837 structures had corresponding PXRD patterns from the initial download of 1,362 patterns. Cross-validation between the DIF and PXRD files confirmed that 745 structures had matching crystal systems and lattice parameters. Since many of the experimental PXRD patterns were measured using Cu K_α radiation (8.04 keV) while our model assumes an energy of 20 keV, we converted the patterns to the desired 2θ range using Bragg's law. This conversion step resulted in 734 structures with patterns that did not contain missing data in the new 2θ range. Of these 734 structures, 240 had complete atom position information, enabling GSAS-II [25] PXRD simulations that yielded peaks consistent with those reported in the DIF files. This validation process required manually determining the origin and nonstandard settings in some cases due to incomplete data. Specifically, many RRUFF entries use nonstandard space group notation that required translation to the full Hermann-Mauguin symbols needed by GSAS-II. For structures in space groups with ambiguous symmetry center locations (Origin 1 and 2 settings), we determined the correct origin through systematic examination of special positions, interatomic distances, and visual inspection of the structure.

We utilized the full set of 734 structures for crystal system and space group classification, but only the subset of 240 structures for lattice parameter regression, as reliable parameter extraction required Niggli reduced cells derived from complete structures rather than from lattice parameters alone. We note that while the RRUFF database is widely regarded as an experimental PXRD database, some entries are calculated powder profiles derived from single crystal data. Our test datasets include 59 such entries among the 734 patterns for classification (8.0%) and 55 among the 240 patterns for regression (22.9%), which we treat as real-world data consistent with their inclusion in RRUFF.

Supplementary Figure 1a, b, and d shows the distribution of crystal systems and space groups in the final ICSD, Materials Project, and RRUFF datasets, respectively, used for crystal system and space group classification. Additionally, Supplementary Figures 2 and 3 show the distribution of lattice lengths and angles, respectively, of each Niggli reduced cell in the final ICSD, Materials Project, and RRUFF datasets used for lattice parameter regression.

5.2 Noise simulation

To realistically simulate noise in synthetic PXRD patterns, we characterized the noise properties of PXRD data from the RRUFF database. Background regions of each pattern were identified and used to estimate noise parameters (Supplementary Figure 4a). From these background regions, we extracted two key noise characteristics: λ_{\max} , which quantifies Poisson noise, and σ_{rel} , which quantifies Gaussian noise on a relative intensity scale. Specifically, σ_{rel} was set equal to the standard deviation of the background regions, while λ_{\max} was set to be the inverse of the mean of the background regions. The parameter λ_{\max} serves as the mean of a Poisson distribution from which noisy intensities are sampled from clean simulated patterns, capturing the counting statistics inherent to X-ray detection. The parameter σ_{rel} represents the standard deviation of Gaussian noise applied to normalized intensities (i.e., after rescaling each pattern to [0,1]), making it a measure of noise relative to the pattern’s maximum intensity rather than on an absolute scale. The distributions of λ_{\max} and σ_{rel} values across the RRUFF dataset are shown in Supplementary Figure 4b-c and f-g, respectively. To validate our noise model, we compared RRUFF patterns at various noise levels with clean simulated patterns to which we applied corresponding amounts of Poisson and Gaussian noise (Supplementary Figure 4d-e and h-i). While experimental patterns contain both Poisson and Gaussian noise components simultaneously (with Gaussian noise appearing dominant), the visual comparison shows that the overall noise characteristics and trends follow expected patterns, supporting the adequacy of our two-step noise model for generating realistic synthetic training data.

The noisy PXRD intensity is obtained through the following sequential steps. First, Poisson noise is applied and the intensity rescaled:

$$I_{\text{Pois}}(2\theta) = \frac{\max(I_{\text{clean}})}{\lambda_{\max}} \cdot \text{Poisson} \left(\lambda_{\max} \cdot \frac{I_{\text{clean}}(2\theta)}{\max(I_{\text{clean}})} \right) \quad (1)$$

Then, Gaussian noise is applied to the normalized intensity:

$$I_{\text{Gauss}}(2\theta) = \frac{I_{\text{Pois}}(2\theta) - \min(I_{\text{Pois}})}{\max(I_{\text{Pois}}) - \min(I_{\text{Pois}})} + \mathcal{N}(0, \sigma_{\text{rel}}) \quad (2)$$

Finally, the pattern is renormalized to [0,1] and rescaled back to the original intensity range:

Parameter	Minimum	Maximum
Sample and instrumental broadening (static)		
Microstrain	500	10,000
Crystallite Size (μm)	0.1	1
U (cdeg ²)	0	3
V (cdeg ²)	-1	0
W (cdeg ²)	0	4
Noise augmentation (dynamic)		
λ_{\max}	1	100
σ_{rel}	10^{-3}	10^{-1}

Table 5: **Parameters for PXRD pattern augmentation.** For each structure, we generated 100 augmented PXRD patterns using GSAS-II by uniformly sampling the sample and instrumental parameters between the given ranges (static augmentation). During training, noise parameters (λ_{\max} , σ_{rel}) were additionally sampled uniformly in the data loader (dynamic augmentation). The unit “cdeg” refers to centidegrees (degrees/100).

$$I_{\text{noisy}}(2\theta) = \left[\frac{I_{\text{Gauss}}(2\theta) - \min(I_{\text{Gauss}})}{\max(I_{\text{Gauss}}) - \min(I_{\text{Gauss}})} \right] \cdot (\max(I_{\text{Pois}}) - \min(I_{\text{Pois}})) + \min(I_{\text{Pois}}) \quad (3)$$

where $I_{\text{clean}}(2\theta)$ is the clean simulated intensity, $I_{\text{Pois}}(2\theta)$ is the intensity after Poisson noise application, $I_{\text{Gauss}}(2\theta)$ is the normalized intensity with Gaussian noise added, $\text{Poisson}(\lambda)$ denotes sampling from a Poisson distribution with mean λ , and $\mathcal{N}(0, \sigma_{\text{rel}})$ denotes sampling from a Gaussian distribution with mean zero and standard deviation σ_{rel} .

During training, noise augmentation was applied dynamically in the data loader by randomly sampling λ_{max} uniformly between 1 and 100 and σ_{rel} uniformly between 10^{-3} and 10^{-1} for each training sample. While these ranges are biased toward noisier samples compared to the empirical distributions shown in Supplementary Figure 4, we found that this bias empirically improved model performance on real experimental data, likely by enhancing the model’s robustness to noise.

5.3 Model architecture

The AlphaDiffract model consists of a feature extractor that takes PXRD diffraction patterns and projects them to the feature space. The extracted features are passed to prediction heads, each of which is specialized to predict one of the target properties.

5.3.1 Feature extractor

The feature extractor is composed of 3 ConvNeXt [23] blocks adapted to 1D. An average pooling layer downsamples the image by a factor of 2 after each ConvNeXt block. The architecture of a ConvNeXt block is shown in Figure 1, where the 2D convolution layers in [23] are replaced with the 1D counterparts, but the key block design features of ConvNeXt, including the inverted bottleneck and the upstream positioned depthwise convolution layer, are preserved. The block employs a residual connection like in ConvNeXt where the input is added to the output of the final pointwise convolution layer. The stem (*i.e.*, non-residual) branch is subject to random drop path [41] with a rate of 0.3. Other parameters, including the input/output channels, kernel size and pooling stride for each block, are listed in Table 6. With an input dimension of 8192, the feature extractor outputs features with a dimension of 560.

5.3.2 Prediction heads

Each quantity (crystal system, space system, *etc.*) is predicted by its own prediction head. A prediction head is a multi-layer perceptron that maps the extractor features to vectors with quantity-specific dimensions. The input, output and hidden dimensions of the prediction heads are shown in Table 7. For classification quantities, the output vectors are passed through a softmax layer to give the predicted probability of each class. For lattice parameters, the outputs are 6-dimensional vectors corresponding to the a , b , c , α , β , and γ of the unit cell’s lengths and angles; the outputs are passed through a sigmoid function and then scaled between a set lower bound and upper bound:

$$y_i = \sigma(p_i)(UB_i - LB_i) + LB_i \quad (4)$$

where i indexes the elements of the 6 lattice parameters, and p_i is the element in the prediction head output corresponding to parameter i . UB_i and LB_i denote the upper and lower bounds and are 0 and 500 Å for lengths and 0° and 180° for angles.

5.4 Loss function

Our overall loss function combines three components tailored to different prediction tasks. For crystal system (CS) and space group (SG) classification, we employ cross-entropy loss for both tasks. The SG loss also optionally includes the Graph Earth Mover’s Distance (GEMD) loss weighted by a hyperparameter μ . For our combined model with lattice parameter regression, we additionally include mean squared error (MSE) loss for lattice parameter (LP) prediction. The batch loss is computed as the average over N samples:

Block	Input channels	Output channels	Kernel size (k)	Pooling stride (s)
1	1	80	100	5
2	80	80	50	5
3	80	80	25	5

Table 6: **Block-level architecture of the feature extractor.**

$$\mathcal{L} = \mathcal{L}_{CS} + \mathcal{L}_{SG} + \mathcal{L}_{LP} = \frac{1}{N} \sum_{i=1}^N \ell^{(i)} \quad (5)$$

where the loss for a single sample is given by:

$$\ell^{(i)} = - \sum_{j=1}^7 y_{CS,j}^{(i)} \log(\hat{y}_{CS,j}^{(i)}) - \sum_{j=1}^{230} y_{SG,j}^{(i)} \log(\hat{y}_{SG,j}^{(i)}) + \mu \sum_{k=1}^{230} \sum_{j=1}^{230} y_{SG,j}^{(i)} D_{jk} \hat{y}_{SG,k}^{(i)} + \frac{1}{6} \sum_{j=1}^6 (y_{LP,j}^{(i)} - \hat{y}_{LP,j}^{(i)})^2 \quad (6)$$

Here, $y^{(i)}$ denotes the ground truth labels or values while $\hat{y}^{(i)}$ represents the model predictions of the i^{th} data sample. The third term represents the GEMD loss, which leverages the hierarchical structure of space groups by penalizing misclassifications based on their distance in the maximal subgroup graph represented by the distance matrix D , where D_{jk} encodes the number of hops between space groups j and k through the maximal subgroup graph.

5.5 Model training

The model is trained using the AdamW optimizer [42] with a learning rate of 2×10^{-4} and weight decay factor of 0.01. We used a cyclic learning rate schedule [43] that linearly increases the learning rate from 10% of its nominal value to the full value over six epochs (a half cycle), then decreases it back, with each subsequent cycle’s amplitude reduced by half. Training for each model was performed on a single NVIDIA H100 GPU using a batch size of 64. 10% of the total training data (from each of ICSD and Materials Project databases) were used as the validation set.

5.6 Uncertainty estimation

We quantify two independent sources of uncertainty in the predictions of our neural network. First, ensemble uncertainty arises from variability across the independently trained model instances. Second, since each of the unique structures in the ICSD and Materials Project datasets is augmented 100-fold with variations in sample and instrument broadening parameters and noise, we define augmentation uncertainty as the variability in predictions across PXRD patterns generated from the same structure. These uncertainties are translated into error bars on the classification accuracy and regression metrics reported in the main text as follows.

5.6.1 Crystal system and space group classification

For each prediction, we first compute the standard deviation of class probabilities across ensemble members, $\sigma_{model}^{(i)}$. We propagate this per-sample uncertainty to the overall accuracy metric using the delta method, computing the standard error as,

$$\sigma_{model} = \frac{1}{N} \sqrt{\sum_{i=1}^N (\sigma_{model}^{(i)})^2}, \quad (7)$$

where N is the total number of samples. The 95% confidence interval is then given by the accuracy $\pm z_{0.975} \cdot \sigma_{model}$, where $z_{0.975} = 1.96$. Next, uncertainty arising from different augmentations is computed by first calculating the fraction of correctly classified augmentations,

$$a^{(j)} = \frac{1}{100} \sum_{k=1}^{100} (y_k^{(j)} = \hat{y}_k^{(j)}). \quad (8)$$

The standard error of the mean accuracy across these structures is then,

$$\sigma_{aug} = \frac{s_a}{\sqrt{n}}, \quad (9)$$

Predicted quantity	Input dimension	Hidden dimension	Output dimension
Crystal system	560	2300 \rightarrow 1150	7
Space group	560	2300 \rightarrow 1150	230
Lattice parameters	560	512 \rightarrow 256	6

Table 7: Dimensions of the MLP prediction heads.

where s_a is the sample standard deviation of $\{a^{(j)}\}$ and $n = N/100$ is the number of unique structures. The 95% confidence interval uses the t-distribution and is given by the accuracy $\pm t_{0.975, n-1} \cdot \sigma_{aug}$.

5.6.2 Lattice parameter regression

We propagate ensemble and augmentation uncertainties to the regression metrics using standard error propagation. Let N denote the total number of test samples and n the number of unique structures, with each structure j having 100-fold augmentation. For each augmented sample i belonging to structure j , the model uncertainty $\sigma_{model}^{(i)}$ represents the standard deviation of predictions across ensemble members. The augmentation uncertainty $\sigma_{aug}^{(j)}$ captures variation in the ensemble-averaged predictions across the 100 augmented patterns for structure j . To estimate errors on each regression metric used to evaluate lattice parameter prediction, we first combine the two uncertainty sources in quadrature,

$$\sigma_{total}^{(j)} = \sqrt{\frac{1}{100} \sum_{k=1}^{100} \left(\sigma_{model,k}^{(j)}\right)^2 + \left(\sigma_{aug}^{(j)}\right)^2}. \quad (10)$$

We then propagate this total uncertainty to each metric using the delta method. For mean absolute error (MAE), the uncertainty is

$$\sigma_{MAE} = \frac{1}{n} \sqrt{\sum_{j=1}^n \left(\sigma_{total}^{(j)}\right)^2}. \quad (11)$$

For mean absolute percentage error (MAPE), the uncertainty scales by the inverse of the true values:

$$\sigma_{MAPE} = \frac{100}{n} \sqrt{\sum_{j=1}^n \left(\frac{\sigma_{total}^{(j)}}{|y^{(j)}|}\right)^2}. \quad (12)$$

For the coefficient of determination (R^2), we use the derivative $\partial R^2 / \partial \hat{y}^{(j)} = -2(\hat{y}^{(j)} - y^{(j)}) / SS_{tot}$, where $SS_{tot} = \sum_{i=1}^n (y^{(i)} - \bar{y})^2$, giving

$$\sigma_{R^2} = \sqrt{\sum_{j=1}^n \left(\frac{2(\hat{y}^{(j)} - y^{(j)})}{SS_{tot}} \sigma_{total}^{(j)}\right)^2}. \quad (13)$$

Here $y^{(j)}$ and $\hat{y}^{(j)}$ denote the true and predicted values for structure j (averaged over its augmentations), respectively.

Data availability

Crystal structures are available from the Materials Project [19] and RRUFF [20] databases (open access) and ICSD [27] (requires license). Model weights and predictions derived from publicly available datasets will be made available upon publication. Full model weights and predictions are available from the authors upon reasonable request.

Code availability

The code used in this study is made available at <https://github.com/AdvancedPhotonSource/OpenAlphaDiffract>.

Acknowledgments

The authors thank Dr. Laurent Chapon for insightful discussions on the application of machine learning methods to crystallographic analysis of PXRD data. This research used resources of the Advanced Photon Source, a U.S. Department of Energy (DOE) Office of Science User Facility operated for the DOE Office of Science by Argonne National Laboratory under Contract No. DE-AC02-06CH11357, and is based on work supported by the U.S. DOE Office of Science-Basic Energy Sciences, under Contract No. DE-AC02-06CH11357.

Author contributions

M.J.C. conceived the study, supervised the research, and contributed to data analysis and manuscript preparation. N.A. developed the symmetry-constrained training approach, led data processing, and contributed to model training and

evaluation, analysis, and manuscript preparation. M.D. led model architecture development and implementation and contributed to data processing, model training and evaluation, analysis, and manuscript preparation. H.S. developed the PXRD simulation pipeline and generated diffraction patterns for training. J.P.H. performed crystal structure data curation and contributed to PXRD pattern generation. A.L. contributed to data processing, analysis, and manuscript preparation. X.Y. conducted benchmarking against prior methods and contributed to analysis. M.P. developed user-facing model deployment tools, containerized the codebase, and performed validation testing. B.H.T. provided crystallographic expertise, performed data curation, contributed to PXRD pattern generation, and assisted with manuscript preparation. All authors reviewed and approved the final manuscript. N.A. and M.D. contributed equally to this work.

Competing interests

The authors declare no competing interests.

Additional information

Correspondence and requests for materials should be addressed to Nina Andrejevic (nandrejevic@anl.gov), Ming Du (mingdu@anl.gov), or Mathew J. Cherukara (mcherukara@anl.gov).

References

- [1] H. M. Rietveld. “A Profile Refinement Method for Nuclear and Magnetic Structures”. In: *Journal of Applied Crystallography* 2 (1969), pp. 65–71. URL: <http://www.ccp14.ac.uk/ccp/web-mirrors/hugorietveld/xtal/paper2/paper2.html>.
- [2] A. Coelho. “Indexing of powder diffraction patterns by iterative use of singular value decomposition”. In: *Journal of Applied Crystallography* 36.1 (2003), pp. 86–95. ISSN: 0021-8898. DOI: doi:10.1107/S0021889802019878. URL: <http://dx.doi.org/10.1107/S0021889802019878>.
- [3] A. Boulton and D. Louer. “Indexing of powder diffraction patterns for low-symmetry lattices by the successive dichotomy method”. In: *Journal of Applied Crystallography* 24 (1991), pp. 987–93. ISSN: 0021-8898. URL: <http://dx.doi.org/10.1107/S0021889802019878>.
- [4] P. E. Werner, L. Eriksson, and M. Westdahl. “TREOR, a semi-exhaustive trial-and-error powder indexing program for all symmetries”. In: *Journal of Applied Crystallography* 18 (1985), pp. 367–70. ISSN: 0021-8898. URL: <http://dx.doi.org/10.1107/S0021889802019878>.
- [5] D. E. Cox, B. H. Toby, and M. M. Eddy. “Acquisition of Powder Diffraction Data with Synchrotron Radiation”. In: *Australian Journal of Physics* 41.2 (1988), p. 117.
- [6] AJ Markvardsen et al. “A probabilistic approach to space-group determination from powder diffraction data”. In: *Foundations of Crystallography* 57.1 (2001), pp. 47–54.
- [7] W B Park et al. “Classification of crystal structure using a convolutional neural network”. In: *IUCrJ* 4.4 (2017), pp. 486–494.
- [8] Pascal Marc Vecsei et al. “Neural network based classification of crystal symmetries from x-ray diffraction patterns”. en. In: *Phys. Rev. B*. 99.24 (June 2019).
- [9] Alexander N. Zaloga et al. “Crystal symmetry classification from powder X-ray diffraction patterns using a convolutional neural network”. In: *Materials Today Communications* 25 (2020), p. 101662. DOI: 10.1016/j.mtcomm.2020.101662.
- [10] Sathya R Chitturi et al. “Automated prediction of lattice parameters from X-ray powder diffraction patterns”. In: *J. Appl. Crystallogr.* 54.6 (2021), pp. 1799–1810.
- [11] Byung Do Lee et al. “Powder X-Ray Diffraction Pattern Is All You Need for Machine-Learning-Based Symmetry Identification and Property Prediction”. In: *Advanced Intelligent Systems* 4.7 (2022).
- [12] Byung Do Lee et al. “A Deep Learning Approach to Powder X-Ray Diffraction Pattern Analysis: Addressing Generalizability and Perturbation Issues Simultaneously”. In: *Advanced Intelligent Systems* 5.9 (2023).
- [13] Nicola Corriero et al. “CrystalMELA: a new crystallographic machine learning platform for crystal system determination”. In: *J. Appl. Crystallogr.* 56.2 (2023), pp. 409–419.
- [14] Juan Iván Gómez-Peralta, Xim Bokhimi, and Patricia Quintana. “Convolutional Neural Networks to Assist the Assessment of Lattice Parameters from X-ray Powder Diffraction”. In: *J. Phys. Chem. A* 127.36 (2023), pp. 7655–7664.

- [15] Jerardo E Salgado et al. “Automated classification of big X-ray diffraction data using deep learning models”. en. In: *Npj Comput. Mater.* 9.1 (Dec. 2023), p. 214.
- [16] Eric A Riesel et al. “Crystal structure determination from powder diffraction patterns with generative machine learning”. en. In: *J. Am. Chem. Soc.* (Sept. 2024).
- [17] Haotong Liang et al. “CRYSPNet: Crystal structure predictions via neural networks”. In: *Physical Review Materials* 4.12 (2020), p. 123802.
- [18] Dejan Zagorac et al. “Recent developments in the Inorganic Crystal Structure Database: theoretical crystal structure data and related features”. In: *Applied Crystallography* 52.5 (2019), pp. 918–925.
- [19] Anubhav Jain et al. “Commentary: The Materials Project: A materials genome approach to accelerating materials innovation”. In: *APL materials* 1.1 (2013).
- [20] Barbara Lafuente et al. “The power of databases: the RRUFF project”. In: *Highlights in mineralogical crystallography* 1 (2015), p. 25.
- [21] Kamal Choudhary. “DiffraGPT: Atomic structure determination from X-ray diffraction patterns using a generative pretrained transformer”. en. In: *J. Phys. Chem. Lett.* (Feb. 2025), pp. 2110–2119.
- [22] Frederik Lizak Johansen et al. “deCIFer: Crystal Structure Prediction from Powder Diffraction Data using Autoregressive Language Models”. In: *arXiv preprint arXiv:2502.02189* (2025).
- [23] Zhuang Liu et al. “A ConvNet for the 2020s”. In: *arXiv* (2022).
- [24] Kaiming He et al. “Deep Residual Learning for Image Recognition”. In: *arXiv* (2015).
- [25] B. H. Toby and R. B. Dreele. “GSAS-II: the genesis of a modern open-source all purpose crystallography software package”. In: *Journal of Applied Crystallography* 46.2 (2013), pp. 544–549.
- [26] Jackson H. O’Donnell et al. “A Scripting Interface for GSAS-II”. In: *Journal of Applied Crystallography* 51.4 (2018), pp. 1244–1250. DOI: 10.1107/S1600576718008075.
- [27] National Institute of Standards and Technology. *NIST Inorganic Crystal Structure Database, NIST Standard Reference Database Number 3*. National Institute of Standards and Technology, Gaithersburg MD, 20899. DOI: 10.18434/M32147. URL: <https://doi.org/10.18434/M32147>.
- [28] James A. Kaduk and Joel Reid. “Typical values of Rietveld instrument profile coefficients”. In: *Powder Diffraction* 26.01 (2011), pp. 88–93. ISSN: 1945-7413. DOI: doi:10.1154/1.3548128. URL: <http://dx.doi.org/10.1154/1.3548128>.
- [29] Pascal Marc Vecsei et al. “Neural network based classification of crystal symmetries from x-ray diffraction patterns”. In: *Physical Review B* 99.24 (2019), p. 245120.
- [30] Gemma de la Flor, Hans Wondratschek, and Mois I Aroyo. “Complete online database of maximal subgroups of subperiodic groups at the Bilbao Crystallographic Server”. In: *Applied Crystallography* 58.2 (2025).
- [31] Mois Ilia Aroyo et al. “Bilbao Crystallographic Server: I. Databases and crystallographic computing programs”. In: *Zeitschrift für Kristallographie-Crystalline Materials* 221.1 (2006), pp. 15–27.
- [32] Ramprasaath R Selvaraju et al. “Grad-cam: Visual explanations from deep networks via gradient-based localization”. In: *Proceedings of the IEEE international conference on computer vision*. 2017, pp. 618–626.
- [33] A. Altomare et al. “EXPO: a program for full powder pattern decomposition and crystal structure solution”. In: *Journal of Applied Crystallography* 32 (1999), pp. 339–340. ISSN: 0021-8898. DOI: 10.1107/S0021889898007729. URL: <https://doi.org/10.1107/S0021889898007729>.
- [34] Vincent Favre-Nicolin and Radovan Cerny. “FOX, ‘free objects for crystallography’: a modular approach to ab initio structure determination from powder diffraction”. In: *Journal of Applied Crystallography* 35.6 (2002), pp. 734–743. ISSN: 0021-8898. DOI: doi:10.1107/S0021889802015236. URL: <http://dx.doi.org/10.1107/S0021889802015236>.
- [35] William I. F. David et al. “DASH: a program for crystal structure determination from powder diffraction data”. In: *Journal of Applied Crystallography* 39.6 (2006), pp. 910–915. ISSN: 0021-8898. DOI: doi:10.1107/S0021889806042117. URL: <http://dx.doi.org/10.1107/S0021889806042117>.
- [36] Stefan Habermehl, Carina Schlesinger, and Martin U. Schmidt. “Structure determination from unindexed powder data from scratch by a global optimization approach using pattern comparison based on cross-correlation functions”. In: *Acta Crystallographica Section B* 78.2 (2022), pp. 195–213. ISSN: 2052-5206. DOI: doi:10.1107/S2052520622001500. URL: <https://doi.org/10.1107/S2052520622001500>.
- [37] Peter W Stephens and Ashfia Huq. “PSSP: An open source powder structure solution program for direct space simulated annealing”. In: *Transactions of the American Crystallographic Association* 37 (2002), pp. 125–142.
- [38] James A. Kaduk. “Use of the Inorganic Crystal Structure Database as a problem solving tool”. In: *Acta Crystallographica Section B* 58.3 Part 1 (June 2002), pp. 370–379. DOI: 10.1107/S0108768102003476. URL: <https://doi.org/10.1107/S0108768102003476>.

- [39] I. David Brown and Brian McMahon. “CIF: the computer language of crystallography”. In: *Acta Crystallographica Section B* 58.3 Part 1 (June 2002), pp. 317–324.
- [40] Shyue Ping Ong et al. “Python Materials Genomics (pymatgen): A robust, open-source python library for materials analysis”. In: *Computational Materials Science* 68 (2013), pp. 314–319.
- [41] Gustav Larsson, Michael Maire, and Gregory Shakhnarovich. “FractalNet: Ultra-deep neural networks without residuals”. In: *arXiv [cs.CV]* (May 2016).
- [42] Ilya Loshchilov and Frank Hutter. “Decoupled weight decay regularization”. In: *arXiv [cs.LG]* (Nov. 2017).
- [43] Leslie N Smith. “Cyclical learning rates for training neural networks”. In: *2017 IEEE winter conference on applications of computer vision (WACV)*. IEEE, 2017, pp. 464–472.

Supplemental Material for "AlphaDiffract: Automated Crystallographic Analysis of Powder X-ray Diffraction Data"

Nina Andrejevic^{1*†}, Ming Du^{1*†}, Hemant Sharma¹, James P. Horwath¹, Aileen Luo¹, Xiangyu Yin¹, Michael Prince¹, Brian H. Toby¹, and Mathew J. Cherukara^{1*}

¹*Advanced Photon Source, Argonne National Laboratory, Lemont, IL 60439, USA*

[†]Co-first authors with equal contribution.

*E-mail: nandrejevic@anl.gov, mingdu@anl.gov, mcherukara@anl.gov

1 Literature survey on deep learning methods for PXRD analysis

1.1 Architecture design

1D convolutional neural networks (CNNs) have been the predominant architectural choice for PXRD analysis [S1–S10]. CNNs are well-suited to PXRD data because they capture both local features (individual peaks) through inductive bias and long-range relationships (peak patterns) through hierarchical downsampling—both critical for structure identification. Typical implementations use CNNs as feature extractors that project PXRD patterns to latent representations, followed by one or more multilayer perceptron (MLP) heads that map features to classification or regression outputs. These extractors commonly employ multiscale architectures with pooling or strided convolutions between blocks to increase receptive field size. However, Salgado *et al.* [S9] found that removing pooling layers while maintaining strided convolutions improved performance on some datasets, attributed to reduced information compression, though at the cost of decreased receptive fields and increased parameters in downstream heads. A key consideration for CNNs in PXRD analysis is shift-equivariance: spatial shifts in input produce corresponding shifts in output. Combined with pooling operations [S11], this can lead to shift-invariance—desirable for image classification but problematic for PXRD, where shifted patterns in 2θ space represent different structures. This issue is mitigated when MLP prediction heads follow CNN extractors, as MLPs are inherently shift-sensitive. Some works [S2, S5, S12] have explored pure MLP architectures to exploit this sensitivity, though results are mixed: Vecsei *et al.* [S2] found MLPs performed better on experimental data but worse on synthetic data compared to CNNs. In practice, MLPs face computational challenges due to large parameter counts and expensive matrix operations. Transformers, highly successful in natural language processing [S13] and computer vision [S14], have seen limited application in PXRD. Lee *et al.* [S5] found transformer-based models underperformed CNNs even with PXRD-specific pretraining, attributing this to transformers' data hunger: without CNN-like inductive biases, they require substantially more training samples. However, recent work on DiffractGPT [S15] demonstrates that large pretrained language models (*e.g.*, Mistral 7B [S16]) can be effectively fine-tuned for PXRD-based lattice and atomic position prediction, suggesting a promising direction for leveraging models pretrained on extensive language data.

1.2 Training data sources and scale

ICSD [S17] and Materials Project [S18] are the primary crystallographic databases used for training. After curation to remove problematic structures, both databases provide large-scale training sets and have been widely adopted [S1–S6, S9, S10, S12]. While ICSD and Materials Project provide simulated data, the RRUFF database [S19] offers predominantly experimental PXRD patterns, serving as a benchmark for model performance under realistic conditions [S2, S6, S9, S10]. The largest reported training set contains 263,000 structures from ICSD and Materials Project [S5]. To model experimental imperfections such as lattice strain and peak broadening, multiple augmented patterns are often generated per structure with varied perturbations. For example, Lee *et al.* [S6] generated 20 augmentations per structure, yielding 3.7 million training samples.

1.3 Prediction targets and model scope

Most works focus on crystal symmetry classification, predicting crystal systems and space groups. Some extend to continuous quantities including lattice parameters [S4, S8, S10, S12, S15] and material properties such as band gap and formation energy [S5]. However, many approaches require separate specialized models for different tasks or structure types. For instance, Chitturi *et al.* [S4] trained seven separate models – one per crystal system – for lattice parameter

prediction, while Lee *et al.* [S5] used distinct models for classification and property regression. While dedicated models simplify training, unified models that predict multiple quantities simultaneously streamline inference workflows.

2 Structure similarity between ICSD and Materials Project databases

To evaluate structural similarity and database overlap, we employed the CrystalNN site fingerprint method [S20] with structural order parameters as implemented in matminer [S21] to characterize each structure in both the ICSD and Materials Project databases. We performed hierarchical clustering, as implemented in scipy [S22], using complete linkage with a Euclidean distance metric on the fingerprints of structures sharing identical composition and space group. Structures were classified as "equivalent" if they belonged to the same cluster within a distance threshold of 0.9, following the convention proposed in the Materials Project documentation [S18]. This analysis enabled us to decompose the combined dataset into structures appearing exclusively in ICSD, exclusively in the Materials Project, or in both databases, with each dataset further subdivided into unique structures and any structural equivalents (Supplementary Figure 1c). This clustering approach revealed that the final curated dataset comprises 65,748 unique ICSD structures, 93,418 unique Materials Project structures, and 39,239 unique structures common to both databases, and that 18,683 ICSD structures, 12,616 Materials Project structures, and 82,545 structures common to both databases are structural equivalents of other structures in their respective datasets.

Reference	Architecture	Training database	Test database	Number of training inorganic structures	Number of training organic structures	Total number of training structures	Total number of training diffraction patterns	Predicted quantities	Remarks
Park <i>et al.</i> [S1]	ID CNN	ICSD	ICSD	120,000	0	120,000	120,000	CS, SG, EG	
Vecsei <i>et al.</i> [S2]	ID CNN, MLP	ICSD	ICSD, RRUFF	114,404	0	114,404	114,404	CS, SG	
Zaloga <i>et al.</i> [S3]	ID CNN	ICSD	ICSD	153,603	0	153,603	–	CS, SG	
Liang <i>et al.</i> [S12]	MLP	ICSD	ICSD	110,813	0	100,000	100,000	BL, SG, LP	After predicting BL, trained separate models to predict SG and LP for each BL. Train/test are split by year of publication.
Chitturi <i>et al.</i> [S4]	ID CNN	ICSD, CSD	ICSD, CSD	~137,000	~825,000	960,000	960,000	LP	Trained a separate model for each CS. Inorganic/organic numbers are calculated from Fig. 1 of cited paper.
Lee <i>et al.</i> [S5]	ID CNN, transformer (structures), MLP (properties)	ICSD, MP	ICSD, MP	263,000	0	263,000	263,000	CS, EG, SG, E_g , E_f , E_h	
Lee <i>et al.</i> [S6]	ID CNN	ICSD	RRUFF	187,131	0	187,131	3,742,620	CS, SG, EG	Listed numbers are based on 20 texture-involving perturbations generated for each structure. A separate dataset of 10 texture-free patterns per structure was also generated.
Corriero <i>et al.</i> [S7]	ID CNN	POW_COD	Private database	21,783	261,223	283,006	283,006	CS	Listed numbers are total data size; train/test ratio unavailable.
Gómez-Peralta <i>et al.</i> [S8]	ID CNN	COD	COD	0	83,000	83,000	332,000	LP	
Salgado <i>et al.</i> [S9]	ID CNN	ICSD	RRUFF	171,006	0	171,006	1,200,000	CS, SG	
Riesel <i>et al.</i> [S10]	ID CNN	MP-20	MP-20, AMCSD, RRUFF	36,185	0	36,185	144,740	CP, LP, NA	Train on MP-20 subset of MP dataset containing only structures with 1-20 atoms in the primitive unit cell.
Choudhary [S15]	Mistral 7B	JARVIS-DFT	JARVIS-DFT	72,990	0	72,990	72,990	LP, AP	
Ours	ID ConvNeXt	ICSD, MP	RRUFF	312,267	0	312,267	31,226,700	CS, SG, LP	

Supplementary Table 1: **Survey of deep learning methods for PXRD analysis.** A survey on the data sources, sizes of training data, and predicted quantities for models that predict crystal structures and material properties from PXRD diffraction patterns. We only include works where the models were trained on a comprehensive collection of structures rather than ones only trained for certain materials systems. “Number of structures” refers to the distinct structures in the training data, while “number of diffraction patterns” means the actual number of samples in the dataset that include all augmented variants. Since multiple augmented variants can be generated from each structure, numbers in this column are greater than or equal to the numbers of structures. “–” means the figures are not explicitly mentioned in the papers and are hard to deduce with certainty. Abbreviations and symbols: CS – crystal system, SG – space group, EG – extinction group, LP – lattice parameters, BL – Bravais lattice, AP – atomic positions, E_g – bandgap, E_f – formation energy, E_h – energy above the convex hull, CP – chemical composition, NA – number of atoms.

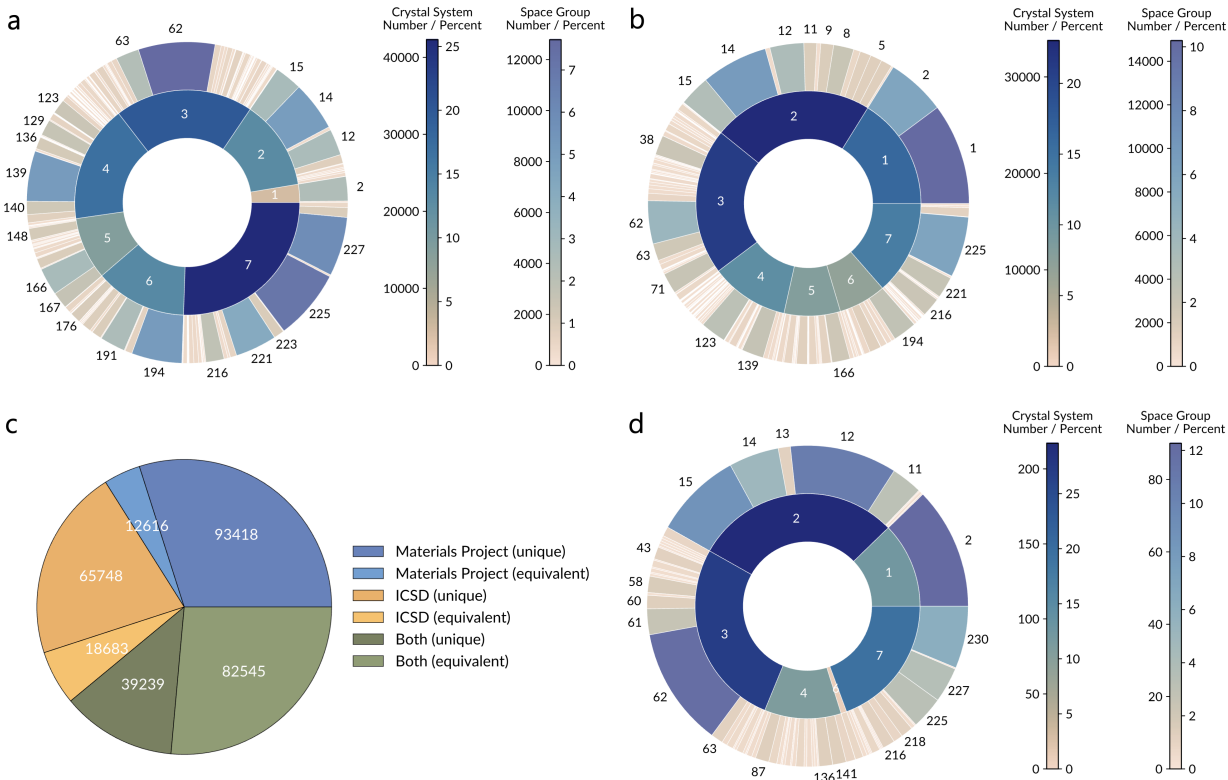
	Model variant	Test data	Metric	Metric value					
				a	b	c	α	β	γ
Choudhary [S15]	DGPT-formula	JARVIS-DFT	MAE	0.17	0.18	0.27	–	–	–
Choudhary [S15]	DGPT-formula	ICSD [†]	MAE	1.72 (1.66)	2.40 (2.28)	4.44 (4.44)	5.00 (5.16)	2.76 (3.34)	9.51 (10.20)
Choudhary [S15]	DGPT-formula	Materials Project [†]	MAE	1.55 (1.48)	2.17 (2.13)	4.36 (4.47)	4.96 (5.45)	2.85 (3.53)	10.11 (9.89)
Choudhary [S15]	DGPT-formula	RRUFF [‡]	MAE	1.72 (1.66)	2.40 (2.28)	4.44 (4.44)	5.00 (5.16)	2.76 (3.34)	9.51 (10.20)
Ours	Cls. + Regr. Ensemble	ICSD [†]	MAE	1.14 ± 0.00	1.33 ± 0.00	2.29 ± 0.01	2.02 ± 0.01	0.61 ± 0.00	2.41 ± 0.01
Ours	Cls. + Regr. Ensemble	Materials Project [†]	MAE	1.22 ± 0.00	1.60 ± 0.00	2.93 ± 0.01	3.66 ± 0.01	1.63 ± 0.00	4.72 ± 0.02
Ours	Cls. + Regr. Ensemble	RRUFF [‡]	MAE	1.37 ± 0.02	1.76 ± 0.02	3.22 ± 0.05	2.95 ± 0.05	2.31 ± 0.03	2.90 ± 0.07
Chitturi <i>et al.</i> [S4]	Full range	ICSD, CSD	MAPE	9.20			–	–	–
Choudhary [S15]	DGPT-formula	ICSD [†]	MAPE	27.11 (26.97)	34.63 (33.32)	41.23 (40.69)	4.88 (5.06)	3.05 (3.66)	9.54 (10.27)
Choudhary [S15]	DGPT-formula	Materials Project [†]	MAPE	23.17 (22.88)	29.59 (28.17)	31.67 (30.06)	5.10 (5.62)	3.15 (3.91)	10.51 (10.31)
Choudhary [S15]	DGPT-formula	RRUFF [‡]	MAPE	22.72 (23.18)	27.92 (25.40)	27.20 (27.38)	4.38 (4.45)	3.81 (4.04)	9.00 (8.68)
Ours	Cls. + Regr. Ensemble	ICSD [†]	MAPE	19.52 ± 0.05	18.54 ± 0.06	21.23 ± 0.08	2.03 ± 0.01	0.66 ± 0.00	2.39 ± 0.01
Ours	Cls. + Regr. Ensemble	Materials Project [†]	MAPE	21.58 ± 0.05	21.92 ± 0.06	24.27 ± 0.08	3.88 ± 0.01	1.83 ± 0.00	5.12 ± 0.02
Ours	Cls. + Regr. Ensemble	RRUFF [‡]	MAPE	22.21 ± 0.31	19.87 ± 0.28	28.42 ± 0.64	3.14 ± 0.06	2.51 ± 0.03	3.06 ± 0.08
Liang <i>et al.</i> [S12]	–	ICSD	R^2	0.56*	0.34*	0.46*	0.43*	0.14*	0.01*
Choudhary [S15]	DGPT-formula	ICSD [†]	R^2	-0.04 (0.03)	0.05 (0.12)	-0.08 (-0.31)	-0.55 (-0.66)	-4.50 (-6.41)	-1.15 (-1.32)
Choudhary [S15]	DGPT-formula	Materials Project [†]	R^2	0.11 (0.12)	-0.02 (0.03)	-0.13 (-0.18)	-0.82 (-1.00)	-2.77 (-3.93)	-1.02 (-1.03)
Choudhary [S15]	DGPT-formula	RRUFF [‡]	R^2	0.04 (-0.02)	-0.35 (-0.19)	-0.04 (-0.14)	-0.89 (-0.77)	-1.28 (-1.11)	-4.85 (-5.06)
Ours	Cls. + Regr. Ensemble	ICSD [†]	R^2	0.58 ± 0.00	0.63 ± 0.00	0.71 ± 0.01	0.70 ± 0.00	0.26 ± 0.00	0.78 ± 0.00
Ours	Cls. + Regr. Ensemble	Materials Project [†]	R^2	0.49 ± 0.00	0.48 ± 0.00	0.49 ± 0.00	0.38 ± 0.00	0.11 ± 0.00	0.45 ± 0.00
Ours	Cls. + Regr. Ensemble	RRUFF [‡]	R^2	0.54 ± 0.01	0.39 ± 0.01	0.25 ± 0.02	0.33 ± 0.02	0.26 ± 0.02	0.18 ± 0.03

Supplementary Table 2: **Lattice parameter prediction errors of AlphaDiffraX and reference models.** Errors are quantified in terms of the Mean Absolute Error (MAE), Mean Absolute Percentage Error (MAPE), and coefficient of determination (R^2). For direct comparison, we limit our analysis to studies that quantify prediction accuracy using regression metrics rather than classification metrics like match rate. Due to the scarcity of works tested on RRUFF, we also list those tested on other datasets for reference only. Error bars represent the aggregated standard deviations in the predictions of the ensemble and augmentations.

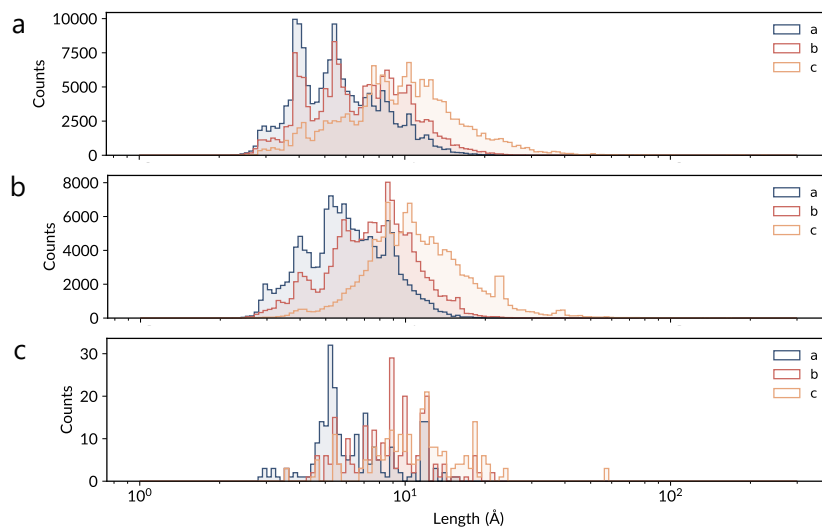
*Weighted average over models specialized for each Bravais lattice.

[†]Evaluated on our validation set data. For inference with the DGPT-formula model, 1000 representative examples from the validation set of each dataset were selected for evaluation. Scores in parentheses refer to results on synthetic PXRD patterns with no added Poisson or Gaussian noise.

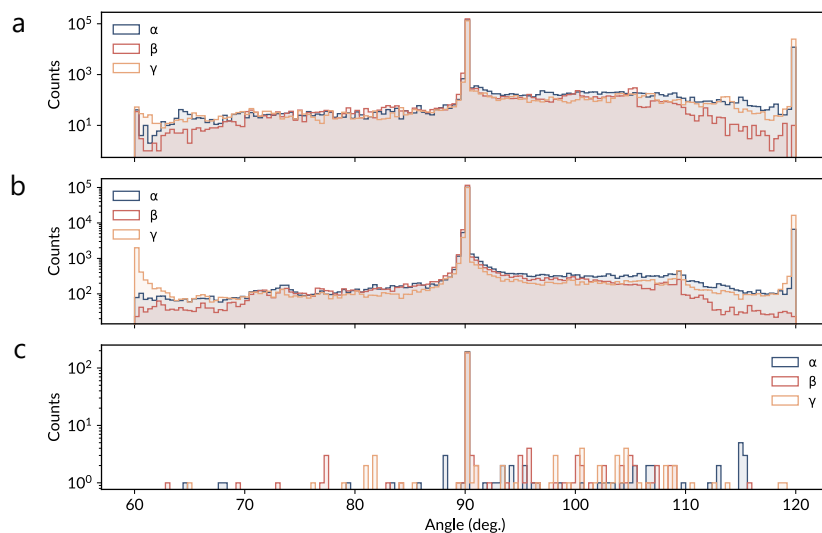
[‡]Evaluated on our test set data.



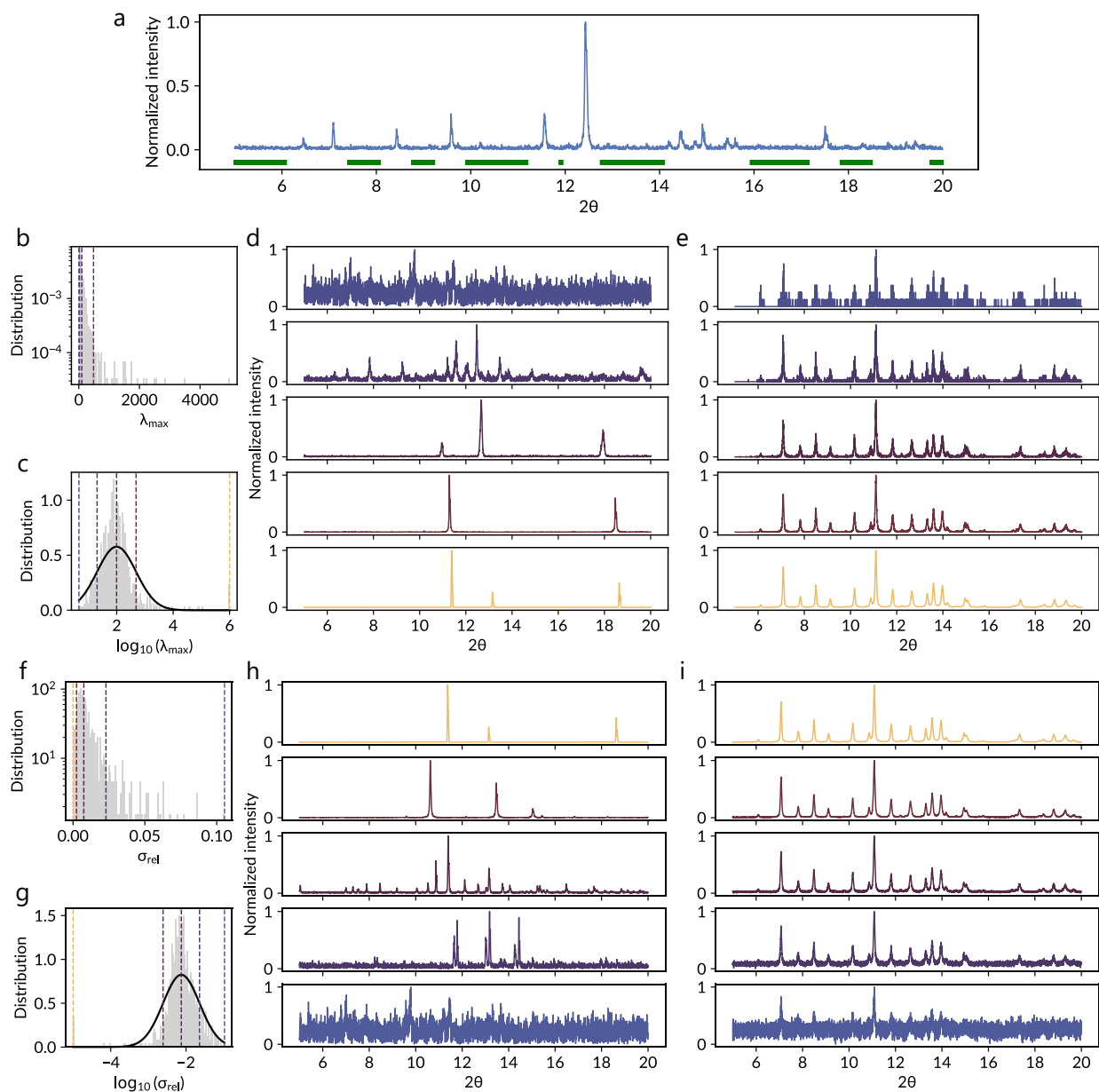
Supplementary Figure 1: **Distribution of crystal systems and space groups across crystallographic databases and structural uniqueness analysis.** **a.** ICSD database showing the distribution of crystal systems (inner ring) and their associated space groups (outer ring) with color intensity indicating the number and percentage of structures. **b.** Materials Project database displaying the same hierarchical representation of crystal systems and space groups. **c.** Pie chart quantifying structural uniqueness and redundancy across ICSD and Materials Project databases, where "unique" structures are crystallographically distinct and "equivalent" structures are identified as similar to a unique structure based on the structure similarity metric detailed in Section 2. **d.** RRUFF database showing crystal system and space group distributions following the same visualization scheme as panels a and b. The seven crystal systems are: 1-triclinic, 2-monoclinic, 3-orthorhombic, 4-tetragonal, 5-trigonal, 6-hexagonal, and 7-cubic. Color bars indicate both absolute counts and relative percentages for crystal systems and space groups in each database.



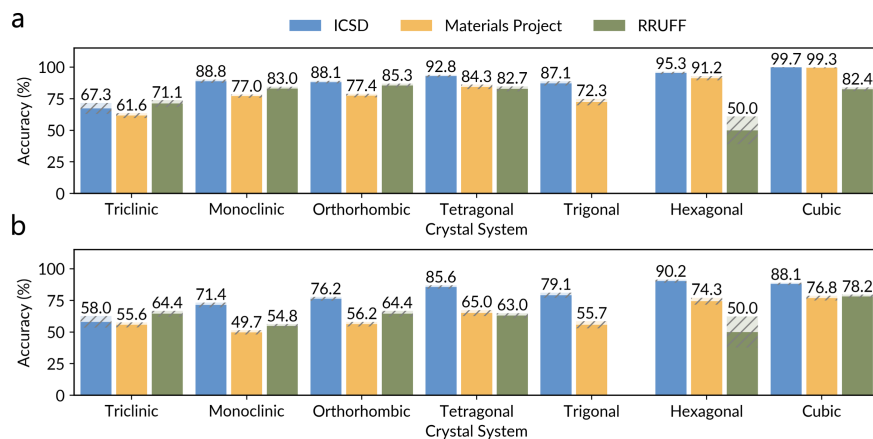
Supplementary Figure 2: **Distribution of lattice lengths across crystallographic databases.** **a.** Histogram of Niggli reduced cell lattice lengths (a , b , c) for structures in the final ICSD dataset. **b.** Corresponding lattice length distributions for structures in the final Materials Project dataset. **c.** Lattice length distributions for structures in the RRUFF dataset used for regression.



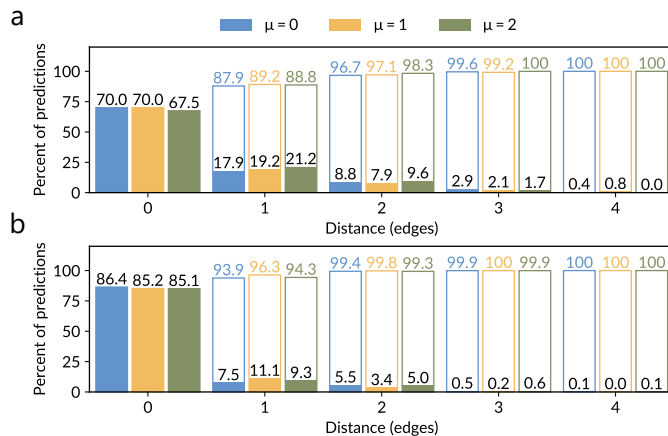
Supplementary Figure 3: **Distribution of lattice angles across crystallographic databases.** **a.** Histogram of Niggli reduced cell lattice angles (α , β , γ) for structures in the final ICSD dataset. **b.** Corresponding lattice angle distributions for structures in the final Materials Project dataset. **c.** Lattice angle distributions for structures in the RRUFF dataset used for regression.



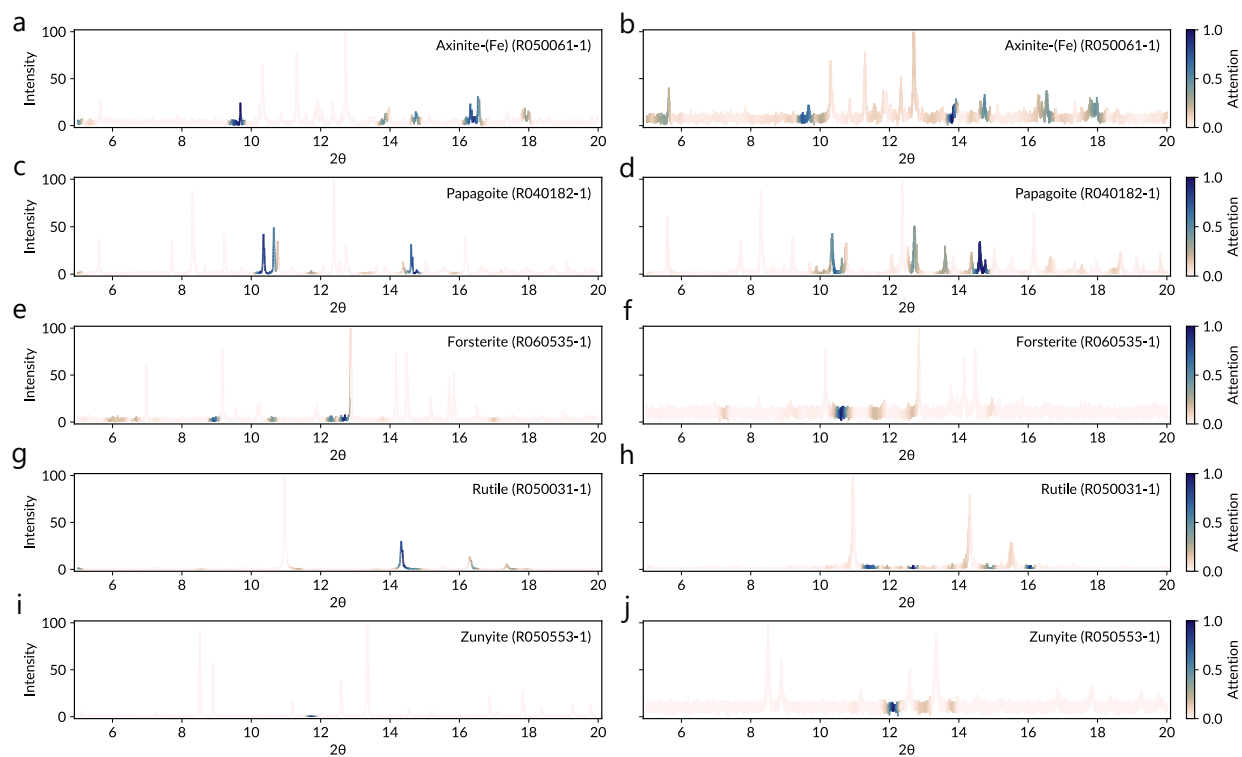
Supplementary Figure 4: **Characterization and simulation of noise in X-ray diffraction patterns.** **a.** Representative PXRD pattern with background regions (underlined in green) used for noise estimation. **b-c.** Distribution of λ_{\max} values from the RRUFF dataset in linear (**b**) and logarithmic (**c**) scales, where λ_{\max} serves as the mean of the Poisson distribution used to sample noise values for simulation. Dashed vertical lines indicate representative λ_{\max} values selected for visualization. **d.** Selected experimental PXRD patterns from the RRUFF database exhibiting representative levels of Poisson noise. **e.** Simulated PXRD patterns with Poisson noise applied by sampling from distributions with means corresponding to the representative λ_{\max} values. **f-g.** Distribution of σ_{rel} values from the RRUFF dataset in linear (**f**) and logarithmic (**g**) scales, where σ_{rel} represents the standard deviation of the Gaussian distribution used to sample noise values for simulation. Dashed vertical lines indicate representative σ_{rel} values selected for visualization. **h.** Selected experimental RRUFF patterns at representative Gaussian noise levels. **i.** Simulated PXRD patterns with Gaussian noise applied at levels corresponding to the representative σ_{rel} values. All PXRD patterns are plotted as normalized intensity versus 2θ (degrees).



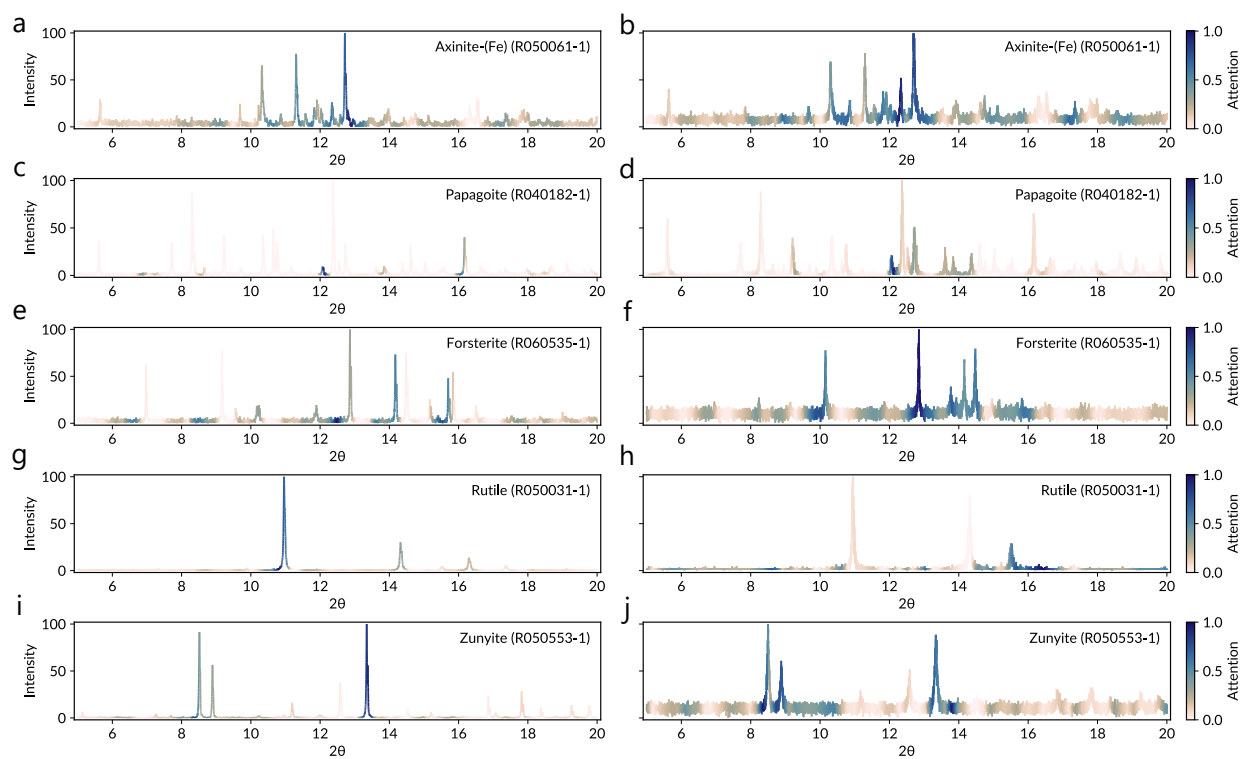
Supplementary Figure 5: **Crystal system and space group classification accuracy per crystal system.** Accuracy (%) of crystal system classification for **a.** crystal system and **b.** space group classification, evaluated on ICSD (blue), Materials Project (orange), and RRUFF (green) datasets. Each group shows performance across the seven crystal systems. Hatched bars indicate combined ensemble model and augmentation uncertainty. Cubic systems achieve the highest accuracy across all datasets, while lower-symmetry systems (Triclinic, Monoclinic) show more variable performance, particularly for Materials Project and RRUFF datasets.



Supplementary Figure 6: **Evaluation of space group predictions from experimental and synthetic RRUFF data.** Distribution of prediction errors as a function of graph distance (number of edges) from the true space group for RRUFF data subset with complete structures available (240 samples) using **a.** experimental and **b.** synthetic PXR D patterns as input. Filled bars show the percentage of predictions at each distance for three different weights applied to the GEMD loss term ($\mu = 0, 1, 2$), while unfilled bars with labeled values indicate cumulative percentages.



Supplementary Figure 7: **GradCAM attention maps of feature importance for crystal system classification.** The left column shows experimental powder PXRD patterns from the RRUFF database, while the right shows synthetic patterns of the same mineral structures. Rows represent different crystal systems: **a-b.** triclinic, **c-d.** monoclinic, **e-f.** orthorhombic, **g-h.** tetragonal, **i-j.** cubic. The color scale indicates normalized attention weights extracted from the last ConvNeXt block.



Supplementary Figure 8: **GradCAM attention maps of feature importance for space group classification.** The left column shows experimental powder PXRD patterns from the RRUFF database, while the right shows synthetic patterns of the same mineral structures. Rows represent different crystal systems: **a-b.** triclinic, **c-d.** monoclinic, **e-f.** orthorhombic, **g-h.** tetragonal, **i-j.** cubic. The color scale indicates normalized attention weights extracted from the last ConvNeXt block.

References

- [S1] W B Park et al. “Classification of crystal structure using a convolutional neural network”. In: *IUCrJ* 4.4 (2017), pp. 486–494.
- [S2] Pascal Marc Vecsei et al. “Neural network based classification of crystal symmetries from x-ray diffraction patterns”. en. In: *Phys. Rev. B*. 99.24 (June 2019).
- [S3] Alexander N. Zaloga et al. “Crystal symmetry classification from powder X-ray diffraction patterns using a convolutional neural network”. In: *Materials Today Communications* 25 (2020), p. 101662. DOI: 10.1016/j.mtcomm.2020.101662.
- [S4] Sathya R Chitturi et al. “Automated prediction of lattice parameters from X-ray powder diffraction patterns”. In: *J. Appl. Crystallogr.* 54.6 (2021), pp. 1799–1810.
- [S5] Byung Do Lee et al. “Powder X-Ray Diffraction Pattern Is All You Need for Machine-Learning-Based Symmetry Identification and Property Prediction”. In: *Advanced Intelligent Systems* 4.7 (2022).
- [S6] Byung Do Lee et al. “A Deep Learning Approach to Powder X-Ray Diffraction Pattern Analysis: Addressing Generalizability and Perturbation Issues Simultaneously”. In: *Advanced Intelligent Systems* 5.9 (2023).
- [S7] Nicola Corriero et al. “CrystalMELA: a new crystallographic machine learning platform for crystal system determination”. In: *J. Appl. Crystallogr.* 56.2 (2023), pp. 409–419.
- [S8] Juan Iván Gómez-Peralta, Xim Bokhimi, and Patricia Quintana. “Convolutional Neural Networks to Assist the Assessment of Lattice Parameters from X-ray Powder Diffraction”. In: *J. Phys. Chem. A* 127.36 (2023), pp. 7655–7664.
- [S9] Jerardo E Salgado et al. “Automated classification of big X-ray diffraction data using deep learning models”. en. In: *Npj Comput. Mater.* 9.1 (Dec. 2023), p. 214.
- [S10] Eric A Riesel et al. “Crystal structure determination from powder diffraction patterns with generative machine learning”. en. In: *J. Am. Chem. Soc.* (Sept. 2024).
- [S11] Min Lin, Qiang Chen, and Shuicheng Yan. “Network In Network”. In: *arXiv [cs.NE]* (Dec. 2013).
- [S12] Haotong Liang et al. “CRYSPNet: Crystal structure predictions via neural networks”. In: *Physical Review Materials* 4.12 (2020), p. 123802.
- [S13] Ashish Vaswani et al. “Attention Is All You Need”. In: *arXiv* (2017).
- [S14] Alexey Dosovitskiy et al. “An Image is Worth 16x16 Words: Transformers for Image Recognition at Scale”. In: *arXiv* (2020).
- [S15] Kamal Choudhary. “DiffractGPT: Atomic structure determination from X-ray diffraction patterns using a generative pretrained transformer”. en. In: *J. Phys. Chem. Lett.* (Feb. 2025), pp. 2110–2119.
- [S16] Albert Q Jiang et al. “Mistral 7B”. In: *arXiv [cs.CL]* (Oct. 2023).
- [S17] Dejan Zagorac et al. “Recent developments in the Inorganic Crystal Structure Database: theoretical crystal structure data and related features”. In: *Applied Crystallography* 52.5 (2019), pp. 918–925.
- [S18] Anubhav Jain et al. “Commentary: The Materials Project: A materials genome approach to accelerating materials innovation”. In: *APL materials* 1.1 (2013).
- [S19] Barbara Lafuente et al. “The power of databases: the RRUFF project”. In: *Highlights in mineralogical crystallography* 1 (2015), p. 25.
- [S20] Nils ER Zimmermann and Anubhav Jain. “Local structure order parameters and site fingerprints for quantification of coordination environment and crystal structure similarity”. In: *RSC advances* 10.10 (2020), pp. 6063–6081.
- [S21] Logan Ward et al. “Matminer: An open source toolkit for materials data mining”. In: *Computational Materials Science* 152 (2018), pp. 60–69.
- [S22] Pauli Virtanen et al. “SciPy 1.0: fundamental algorithms for scientific computing in Python”. In: *Nature methods* 17.3 (2020), pp. 261–272.